An ensemble-based data assimilation system for forecasting variability of the Northwestern Pacific ocean

Yasumasa Miyazawa[1] · Max Yaremchuk[2] · Sergey M. Varlamov[1] · Toru Miyama[1] · Yu-Lin K. Chang[1] ·
Hakase Hayashida[1]

Abstract

An adjoint-free four-dimensional variational (a4dVar) data assimilation (DA) is implemented in an operational ocean forecast system based on an eddy-resolving ocean general circulation model for the Northwestern Pacific. Validation of the system against independent observations demonstrates that fitting the model to time-dependent satellite altimetry during a 10-day DA window leads to substantial skill improvements in the succeeding 60-day hindcast. The a4dVar corrects representation of the Kuroshio path variation south of Japan by adjusting the dynamical balance between amplitude/wavelength of the meander and flow advection. A larger ensemble spread tends to reduce the skill in representing the observed sea surface height anomaly, suggesting that it is possible to use the ensemble information for quantifying the forecast error. The ensemble information is also utilized for modification of the background error covariance (BEC), which improves the accuracy of temperature and salinity distributions. The modified BEC yields the skill decline of the Kuroshio path variation during the 60-day hindcast period, and the ensemble sensitivity analysis shows that changes in the dynamical balance caused by the ensemble BEC result in such skill deterioration.

Keywords Operational ocean forecast system · Satellite altimetry · 3dVar · a4dVar · Kuroshio large meander ·
Ensemble forecast

1 Introduction

Data assimilation (DA) combines the output of numerical models and observations to estimate the oceanic state used as initial conditions for predicting ocean variability. The error property for models and observations governs the skill of the DA products. One of the underlying principles of DA algorithms is the representation of the background error covariance (BEC) that describes the model error statistics. Practical methods dealing with realistic ocean general circulation models (OGCMs) have initially implemented stationary and isotropic empirical functions to simulate BEC under specific assumptions such as optimal interpolation (OI) and three-dimensional variational (3dVar) methods (Ezer and Mellor 1994; Bell et al. 2009). To represent non-stationary and flow-dependent BEC, various favors of the Kalman Filter (KF) have been applied to OGCMs (e.g., Hirose et al. 2005; Ohishi et al. 2023). Four-dimensional variational (4dVar) methods have been implemented in OGCMs to allow implicit representation of BEC evolution (e.g., Usui et al. 2015). In the recent decades, model ensemble approaches combined with KF and 4dVar have been applied to OGCMs to effectively account for the BEC evolution in DA algorithms (Yaremchuk et al. 2016, 2017; Pasmans et al. 2020).

To investigate reproducibility and predictability of the Northwestern Pacific Ocean current variations particularly the Kuroshio path variations south of Japan, within a research framework of the Japan Coastal Ocean Predictability Experiment (JCOPE), we have developed a series of forecast systems. These systems are based on an eddy-resolving OGCM that was initially used for simulating the

Responsible Editor Xiaopei Lin.

✉ Yasumasa Miyazawa
miyazawa@jamstec.go.jp

[1] Application Laboratory, Japan Agency for Marine-Earth Science and Technology, 3173-25 Showa-machi, Kanazawa-ku, Yokohama 236-0001, Japan

[2] US Naval Research Laboratory, Stennis Space Center, MS, USA

Northwestern Pacific Ocean (Miyazawa et al. 2004). While the products of the system have been used extensively in scientific studies (Fujii et al. 2017) and industrial/commercial applications (Sato and Horiuchi 2022), we have been exploring ways to improve the skills of the products. The DA techniques applied for initialization of modeled oceanic conditions include single-variable OI (Miyazawa et al. 2005), multivariate OI (Miyazawa et al. 2008), 3dVar (Miyazawa et al. 2009), and multi-scale 3dVar (ms3dVar) methods (Miyazawa et al. 2017; hereinafter M17) modified for mitigating low-temperature bias due to DA of the satellite sea surface temperature (SST) (Miyazawa et al. 2019).

Recently we have introduced an adjoint-free 4dVar (a4dVar) (Yaremchuk et al. 2017) hereinafter Y17, and demonstrated that the a4dVar scheme outperformed the m3dVar scheme in simulating an event of the Kuroshio meander variation south of Japan that occurred in 2017 using a regional OGCM covering a limited domain just south of Japan (Miyazawa et al. 2020; hereinafter M20). The a4dVar is designed to incorporate time-dependent observation information that is not represented by ms3dVar, as demonstrated by M20.

Here we introduce the a4dVar scheme into an operational Northwestern Pacific system, motivated by the preliminary implementation of the same scheme in M20. As the horizontal resolution and coverage of the system differ significantly from those of M20, an updated sensitivity study of the BEC parameters is necessary for implementation.

We examine the possible relationship between simulation skill and generated ensemble spread by using ensemble simulations based on the model-data misfits and dynamical evolution of the model generated by the a4dVar method (Y17). This allows us to utilize the ensemble spread information for quantifying the forecast errors. Also, we employ ensemble information for modification of the BEC by including the sample covariance estimates, to potentially improve the skill through flow-dependent error covariance information.

For a targeted period from March to December 2020, cold eddies were frequently detached from the tip of the Kuroshio Large Meander (KLM) cold core. In early October, a large eddy was shed from the meander, causing the KLM to temporally disappear until it re-developed in December (see the information provided by the Japan Coast Guard; https://www1.kaiho.mlit.go.jp/KANKYO/KAIYO/qboc/index_E.html).

By applying a4dVar to this active period of the Kuroshio path variation, we investigate the feasibility of utilizing time-dependent information represented by the satellite sea surface height anomaly (SSHA) data. The ocean state forecast could move to spatiotemporally higher resolution (less than 1/12º and hourly). According to Miyazawa et al. (2021), the daily-updated ms3dVar, with a few days long DA window assimilating higher-resolution satellite data into a higher-resolution model, is effective for estimating oceanic front variability with a time scale shorter than 10 days. In the present study, using a lower resolution model, we explore the impact of dynamically consistent a4dVar initialization and ensemble prediction with a 10-day DA window on the longer-term weekly-to-monthly forecast of the ocean variability on larger spatial and longer temporal scales, including the Kuroshio meander propagation and eddy detachment.

Although the adjoint-based 4dVar framework has been implemented in similar operational systems (e.g., Usui et al. 2015), and extended to the ensemble 4dVar formulation by additionally computing the ensemble BEC (e.g., Pasmans et al. 2020), this study discusses the utilization of the a4dVar ensemble simulations for uncertainty estimation and forecast skill improvement.

The paper is organized as follows. In the next section, we describe the method and data. Then, in Sect. 3.1, we present the results of parameter sensitivity experiments based on the validation of system performance against independent observations. In Sect. 3.2, we describe the dynamical effects of the a4dVar scheme on the simulated Kuroshio path variations south of Japan. Section 3.3 and 3.4 provide the analyses of the generated ensemble regarding possible spread-skill relations and the ensemble background error covariance. Sections 4 and 5 are devoted to discussion and summary, respectively.

2 Methods and data

2.1 Ocean model

The JCOPE-T OGCM (Varlamov and Miyazawa 2021) is used as the dynamical constraint to the system. Since the targeted phenomena exclude tidally-driven sea level and flow variations, an offshore (non-tidal) version of JCOPE-T is used for simulations. The model covers a Northwestern Pacific region between 10.5°-62°N and 108°-180°E with a resolution of 1/12°, similar to JCOPE2 (Miyazawa et al. 2009) and JCOPE2M (M17), and 46 active vertical layers based on a generalized sigma coordinate formulation (Mellor et al. 2002).

The above-described 1/12° model was embedded with one-way nesting in a lower-resolution model with a spatial grid of approximately 1/4° and 20 layers, covering most of the Pacific (30°S-62°N and 100°E-90°W). At the lateral boundaries, the lower-resolution model was forced by the monthly climatological temperature and salinity data World Ocean Atlas 2001 (WOA01) (Conkright et al. 2002) with zero ambient velocity.

The mixed layer physics is represented by Mellor-Yamada- Nakanishi- Niino- Furuichi's turbulence parameterization (Nakanishi and Niino 2009; Furuichi et al. 2012). Horizontal viscosity and diffusivity are represented by biharmonic operators multiplied by a Smagorinsky-type coefficient with a constant parameter of 0.1. To stabilize the calculation, we adopt a minimum value of biharmonic diffusion constant of 10^9 m^4s^{-2}.

The atmospheric forcing data include radiation and latent/sensible heat fluxes that are applied at sea surface through the bulk formulae proposed by Li et al. (2010). The short-wave radiation penetrates into the subsurface layer with a 23 m depth scale assuming the Jerlov's water type I (Paulson and Simpson 1977), and the part penetrating below the bottom is ignored in the areas shallower than 23 m. The atmospheric data required for calculation of the bulk formulae are obtained from the National Centers for Environmental Prediction Climate Forecast System (NCEP-CFS) Version 2 (Saha et al. 2014). Freshwater flux is applied at the sea surface to represent the effects of precipitation and evaporation. The freshwater flux caused by the discharge of small rivers is represented as the enhanced precipitation along the coasts over a strip of land 80 km wide (M17). The climatological monthly freshwater volume flux from the only two large rivers, Changjiang and Amur, is represented in the model by the freshwater volume fluxes in the grid cells located at the river mouths.

The lower-resolution North Pacific model was spun up from 1986 to 2020 from the motionless state and temperature/salinity climatology (WOA01). The higher-resolution Northwestern Pacific model was spun up for the same period from the same initial conditions with one-way nesting by the lower-resolution model.

2.2 Adjoint-free 4dVar system

The ensemble-based forecast system (JCOPE-a4dVar) has been developed using the a4dVar method particularly designed for assimilating satellite altimetry (M20). JCOPE-a4dVar creates ensemble members from the first guess initial condition produced by the ms3dVar DA method (M17). Both a4dVar and ms3dVar assimilate the along-track SSHA (Ssalto/Duacs altimeter products) and the synthetic merged sea surface temperature data (MGDSST; Kurihara et al. 2006). In addition, ms3dVar assimilates high-resolution satellite sea surface temperature (Himawari-8) and in situ temperature-salinity profile data (Global Temperature and Salinity Profile Programme (GTSPP). The a4dVar algorithm is designed for mainly extracting the time-dependent information on the oceanic variability from SSHA observations during the DA window (M20). The length L of the DA window is 10 days, which is a repeat cycle of the Jason-series satellite altimeter. All SSHA data within the DA window are assimilated daily whereas MGDSST data are assimilated only at the time of the initialization. Averaged numbers of the assimilated data points for SSHA and SST are approximately 110,000 and 42,000, respectively per the 10-day DA window. The observation errors in assimilating SSHA and MGDSST are fixed at 0.1 m and 2 °C, respectively. A detailed description of the a4dVar algorithm can be found in Appendices 1–3 in M20. We have adopted parameter values similar to those used in the previous studies (Y17: M20), and made slight adjustments based on the results of preliminary sensitivity experiments. Table 1 provides a summary of the parameters used in the present study for reference.

The ensemble members are created at each iteration of the a4dVar cost function minimization using the combined information on the model dynamics and model-data misfit, which is represented as $N \times 2(L+1)$ matrix,

$$X = \{x_{t=0}, s_{t=0}, x_{t=1}, s_{t=1}, \ldots, x_{t=L}, s_{t=L}\} \tag{1}$$

$x_{t=n}$ and $s_{t=n}$ are the model state and data misfit smoothed by the background error covariance (Eq. (30) in M20) with a dimension of the control variables N at a time n. The ensemble perturbations are defined by the eigenvectors of the generalized eigenvalue problem, $\mathbf{XX}^t\mathbf{E} = \mathbf{BE\Lambda}$ (Eq. (27) in M20), where $\mathbf{E}$ and $\mathbf{\Lambda}$ denote an eigenvector matrix of size $N \times 2(L+1)$, and a diagonal eigenvalue matrix of size $2(L+1) \times 2(L+1)$, respectively. Here we use maximum $2(L+1)$ eigenvectors for generating perturbations. The

Table 1 Parameters used in the a4dVar implementation

Parameters in the a4dVar operation	
DA time window length: L	10 (day)
Ensemble size: $m_s = 2(L+1)$	22
Iteration count	10
Perturbation magnitude parameter: ε	0.01
The relative weight of the model snapshots in the hybrid ensemble: α	0.1
Parameters in the background error covariance	
Threshold standard deviation values in the BEC masking	$M(T) = 0.5$ (°C), $M(S) = 0.05$ (psu), $M(\mathbf{u}) = 0.1$ (m/s), $M(\zeta) = 0.05$ (m)
Horizontal decorrelation scales in the diffusion operator: R_{o1}, R_{o2}	$R_{o1} = R_{o2} = 36$ km
Scalar constant controlling the overall magnitude of simulation errors: c	0.2, 0.3, 0.4, 0.5 (see Table 2)
Relative magnitude of the unbalanced components: β	0.1
Parameters in the observation error covariance	
Observation errors SSH, SST, T, S	Error (SSH) = 0.1 (m), Error (SST) = 2 (°C), Error (T/S): Fig. 4 in Miyazawa et al. 2020

ensemble size m_s is thus determined as $m_s = 2 (L+1)$ using the DA window length L (day). The correction to the first guess initial condition is iteratively made as the weighted sum of m_s (=22) ensemble perturbations at each iteration. The number N of control variables (temperature, salinity, horizontal velocity components, SSH) is approximately 4×10^7. For each DA window, the number of iterations is fixed at 10, because the reduction of the cost function is slowed down after 10 iterations in most cases.

Assimilation of SSHA observations requires the mean SSH to evaluate the anomalies. We use the temporal mean SSH of the ocean reanalysis JCOPE2M for a period from 1993 to 2012, which is the same as the reference period of the SSH anomalies provided by the Copernicus Marine and Environment Monitoring Service (CMEMS). We further correct the mean SSH by subtracting 20 cm from the original one by considering the difference of area mean SSH between JCOPE2M driven by the NCEP/NCAR winds and JCOPE-T driven by NCEP-CFS winds. Also, we exclude the SSHA observations with absolute magnitudes larger than 0.8 m from the assimilation process. The fitting to such a large SSHA results in localized anomalous temperature/salinity structures around the Kuroshio Extension front, even though the percentage of such large amplitude SSHA is less than 1%.

The most critical part of the a4dVar system is the BEC matrix **B** describing the uncertainty of model simulation in the DA process. The background error covariance in the JCOPE-a4dVar system is represented by the $N \times N$ matrix whose action on a state vector is computed by sequence of linear operations,

$$\mathbf{B} = c\mathbf{LVCVL}^T \tag{2}$$

Here c denotes a scalar constant controlling the overall magnitude of simulation errors in the cost function, **L** is the linear operator describing hydrostatic and geostrophic balances (e.g., Y17; M20), and the superscript T denotes transposition of a matrix. **V** is a diagonal matrix representing three-dimensional distributions of the background error magnitudes for each control field (temperature T, salinity S, horizontal velocities u, and SSH ζ). **C** stands for the correlation operator. This operator can be specified either by

Table 2 Description of sensitivity experiments for parameters c and **C** in Eq. (1)

	c	C
DIF5	0.5	$\mathbf{C_d}$
DIF4	0.4	$\mathbf{C_d}$
DIF3	0.3	$\mathbf{C_d}$
DIF2	0.2	$\mathbf{C_d}$
ENS2	0.2	$\mathbf{C_{eh}}$

solving the horizontal diffusion equation (e.g., Y17; M20, hereinafter denoted by $\mathbf{C_d}$), or derived from the ensemble.

The diagonal elements of **V** related to the unbalanced part of the respective fields in **B** (Eq. 1) were defined as standard deviations calculated from the ocean reanalysis product JCOPE2M and capped from above by a certain threshold value M. After conducting a number of preliminary experiments, the threshold values were determined as $M(T) = 0.5$ (°C), $M(S) = 0.05$ (psu), $M(u) = 0.1$ (m/s), $M(\zeta) = 0.05$ (m), respectively, while the horizontal decorrelation scale which defines the structure of $\mathbf{C_d}$ was set to 4 grid steps (approximately 36 km). At the start of development, we applied 8 grid steps (72 km) for T/S (R_{o1}) and 4 grid steps (36 km) for u/v/ζ (R_{o2}) based on the assumption that $R_{o1} > R_{o2}$ (Y17; M20). Subsequently, we changed the grid steps for R_{o1} to 4 (36 km) and kept it fixed because further reduction of R_{o2} did not result in significant skill changes. In the current configuration, which targets mesoscale phenomena primarily governed by the geostrophic dynamics, the difference between R_{o1} and R_{o2} would not significantly affect the resulting skills. In the vertical, the background errors were assumed to be uncorrelated.

We examine the forecast skill dependence on the formulation of the correlation operator in Eq. (2) by augmenting **C** with the ensemble-generated correlation operator $\mathbf{C_e}$ given by

$$\mathbf{C_e} = \mathbf{diag(B_e)}^{-1/2} \mathbf{B_e diag(B_e)}^{-1/2}; \mathbf{B_e} = \mathbf{C_1}(s_e) \circ \mathbf{XX}^T \tag{3}$$

Here $\mathbf{C_1}$ (s_e) is the $N \times N$ localization matrix (Gaspari and Cohn 1999) characterized by a horizontal localization scale s_e (measured in grid steps),. **X** is the $N \times m$ matrix of the ensemble perturbations sampled from the results for the previous DA window (see Sect. 2.4), and ∘ denotes the Schur (elementwise) product. **diag( )** denotes the $N \times N$ diagonal matrix with the diagonal elements of the argument. Several sensitivity experiments were conducted on parameter c, as well as the diffusion and ensemble BEC operators (Table 2).

Considering the deficiency in the ensemble statistics due to the limited ensemble size and model errors (Anderson and Anderson 1999), which results in the underestimate of the error variance (Whitaker and Hamill 2012), we apply a hybrid form of the diffusion and ensemble operators ($\mathbf{C_{eh}}$) depending on the variability of the SSH ensemble spread $S(x) = STD[\zeta(\mathbf{x})]$, where STD stands for standard deviation of the ensemble at the location **x**. We consider the resulting SSH ensemble spread $S(x)$ as a proxy for the potential error variance. To discard locations with the low ensemble spread, we define a masking operator $\mathbf{M} = \mathbf{diag}[\theta(S(\mathbf{x}) - S_0)]$, where θ is the Heaviside function and $S_0 = 1$ cm is the threshold value of the spread, so that the hybrid operator is explicitly given by

Table 3 Skill score indices (SSIs) averaged over 2 DA window periods (April and October). Numbers in bold font denote values of the scores independent from DA

	SSHA	MGDSST	SLA	KPA	DFV	IT	IS	MEAN
FGS	0.777	0.998	**0.605**	**0.941**	**0.626**	**0.864**	**0.804**	0.802
DIF5	0.882	0.999	**0.616**	**0.973**	**0.691**	**0.866**	**0.754**	0.825
DIF4	0.878	0.999	**0.622**	**0.972**	**0.682**	**0.866**	**0.751**	0.825
DIF3	0.867	0.999	**0.622**	**0.972**	**0.682**	**0.879**	**0.813**	0.833
DIF2	0.852	0.999	**0.636**	**0.968**	**0.664**	**0.859**	**0.757**	0.819
ENS2	0.848	0.999	**0.629**	**0.966**	**0.672**	**0.880**	**0.782**	0.825

Table 4 As in Table 3 except for hindcast periods from 11-day after to 70-day after the initialization

	SSHA	MGDSST	SLA	KPA	DFV	IT	IS	MEAN
FGS	**0.581**	**0.998**	0.450	0.904	0.541	0.780	0.684	0.705
DIF5	**0.617**	**0.998**	0.650	0.924	0.567	0.795	0.649	0.742
DIF4	**0.621**	**0.998**	0.668	0.919	0.574	0.805	0.680	0.752
DIF3	**0.599**	**0.998**	0.648	0.950	0.556	0.800	0.688	0.748
DIF2	**0.585**	**0.998**	0.594	0.922	0.562	0.778	0.695	0.733
ENS2	**0.609**	**0.998**	0.488	0.906	0.559	0.803	0.717	0.725

$$\mathbf{C_{eh}} := \mathbf{M C_e M} + \ (\mathbf{I - M}) \, \mathbf{C_d} \, (\mathbf{I - M}) \qquad (4)$$

where $\mathbf{I}$ is the identity matrix. The regions with the ensemble spread exceeding S_0 (see Fig. 1c for a case on 10 October 2020) are characterized by the strong ocean current and mesoscale eddy activities, which could involve the flow-dependent error statistics.

The correlation operators' hybrid form (Eq. 4) differs slightly from the traditional formulation of the weighted sum of covariance matrices (Hamill and Snyder 2000) to maintain symmetry in the resulting hybrid matrix $\mathbf{C_{eh}}$. Since we find that the skills of the a4dVar system developed in the present study are sensitive to the background error magnitude matrix $\mathbf{V}$ in (Eq. 1), here we examine the sensitivity of the normalized covariance (correlation) operator $\mathbf{C}$.

Note that the full hybrid form of the operator (Eq. 4) was not used in the orthogonalization of the ensemble perturbations (Y17; M20) but the diffusion operator alone was applied to this part.

2.3 Skill estimation

The observation data for the validation include satellite altimetry (SSHA), MGDSST, drifter velocities, sea level at tide gauge stations, Kuroshio path locations reported by Japan Coast Guard, and in situ temperature/salinity at 100 m depth. Apart from SSHA and MGDSST, all these data types are not assimilated, and, therefore, are independent from the simulation within both the DA window and the succeeding 60-day hindcast period.

We evaluate simulation skills using the skill score index (SSI) proposed by Willmott (1981). SSI for each observation type is calculated in slightly different manner depending on the sampling density/frequency of the observations. SSI is defined as,

$$SSI = 1 - \left\langle (m - o)^2 \right\rangle \Big/ \left\langle (|m - \langle o \rangle| + |o - \langle o \rangle|)^2 \right\rangle \qquad (5)$$

where m and o denote the model and observation data, respectively, and the angular brackets denote averaging over the respective space-time subdomains.

SSIs for SSHA, MGDSST, and for the zonal/meridional drifter velocities (DFV) are calculated daily with horizontal average over the model region. Daily velocity data are calculated from drifter locations compiled by the Drifter Assembly Data Center (DAC) at the Atlantic Oceanographic, and Meteorological Laboratory (AOML). These data are quality-controlled and interpolated to 6-hourly intervals using the optimal interpolation (Lumpkin and Centurioni 2019). Temporal mean values of the daily SSIs are shown in Tables 3 and 4.

Sea level data are available at tide gauge stations around the Japanese coasts. We compare the modeled and observed sea level data at 10 tide gauge stations (AB: Aburatsu, TS: Tosashimizu, MR: Muroto, KS: Kushimoto, UR: Uragami, MJ: Miyakejima, HJ: Hachijojima, SA: Saigo, S0: Sado, FK: Fukaura) shown in Fig. 1. We applied barometric correction to the hourly tide gauge data assuming 1 hPa = 0.01 m (Kawabe 1989). The tide-killer filter (Hanawa and Mitsudera 1985) was also applied to the hourly data to obtain sea level variations mainly associated with the ocean current variability. The sea level variations at the stations along the southern (northern) Japanese coastlines are related to the Kuroshio (Tsushima warm current) variations (Kawabe 1989). Sea level data are converted to anomalies by subtracting the temporal means. SSI of the sea level anomaly

Fig. 1 A snapshot of SSH (m, shades) on 9 April 2020 initialized by the a4dVar case DIF3. The blue curve is the SSH = 0.15 cm contour between 130° to 140°E. The Kuroshio path location reported by the Japan Coast Guard is shown in black. Red circles indicate locations of the tide gauge stations used for the validation and black squares indicate the regions KRS and KRE (see the text for detailed descriptions)
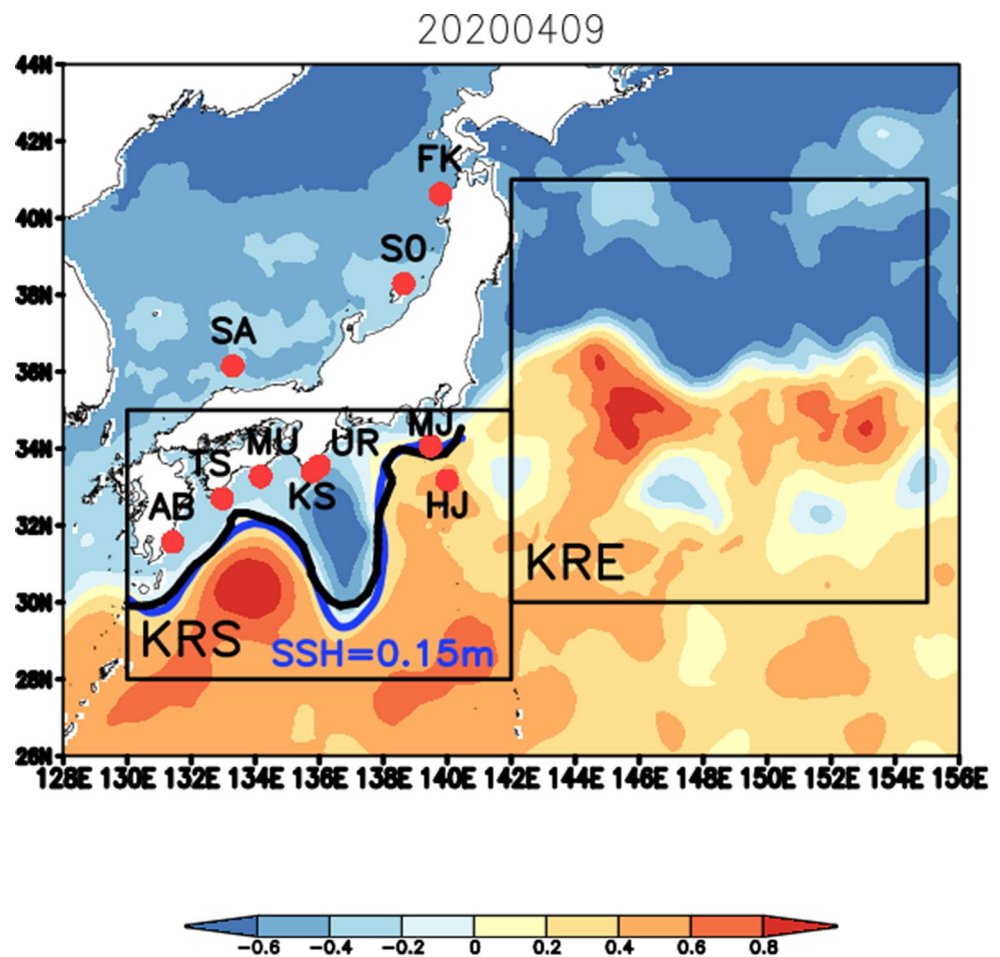
data (SLA) at each station is calculated by applying temporal average. SSI values averaged among the all the stations are shown in Tables 3 and 4 for the skill evaluation.

The Kuroshio path locations reported by the Japan Coast Guard (e.g., black curve in Fig. 2) are compared with those simulated by the model. The Kuroshio path of the model is defined as the 0.15 m SSH contour (e.g., blue curve in Fig. 2). SSI of the Kuroshio path locations (KPA) is calculated for each case by applying spatial average within the longitude range between 130° to 140°E, and the temporal averages are shown in Tables 3 and 4.

In situ temperature and salinity at 100 m depth provided from GTSPP is also compared with the model temperature and salinity. Since distributions of the observed temperature and salinity in various subregions differ considerably, SSIs (IT and IS) are evaluated for each subregion depending on the water mass property by applying horizontal and temporal average (Tables 3 and 4). The subregions are specified similar to the ms3dVar study (see Fig. 2 in M17).

2.4 The ms3dVar and a4dVar experiments

We produced the first guess data by applying ms3dVar for a period from March to December 2020. The a4dVar operation was performed for two 10-day window periods: 9 to 19 April (April period) and 10 to 20 October (October period). KLM was maintained throughout the April and its succeeding 60-day periods. In contrast, KLM disappeared owing to the shedding of a large cold core ring from the tip of KLM in the October period. After that a trigger meander that formed southeast of the Kyushu Island propagated eastward for a succeeding period from October to December, and KLM again appeared through amplification of the trigger meander. Note that the first guess runs failed to predict the persistence of the KLM in April and the eastward propagation of the trigger meander in October.

We performed the a4dVar experiments with selected perturbed parameters c and $\mathbf{C}$ in Eq. (2) for both April and October periods (Table 2). The first guess and a4dVar-corrected initial conditions on 9 April and 10 October were used for 70-day simulation runs. Since the surface forcing and lateral boundary conditions were created from the atmospheric reanalysis products (NCEP-CFS) and the low-resolution

model runs were driven by the same atmospheric forcing, hereinafter these 70-day runs are referred as 'hindcasts'. The hindcasts are examined in terms of predictability of the model trajectories initialized by the ms3dVar and a4dVar DA techniques. The SSIs calculated for the hindcasts of the April and October periods in all cases are shown in Tables 3 and 4.

C_e in Eq. (4) for the ensemble operator case ENS2 were calculated using the ensemble simulation data on April 9 for the April period (and on October 10 for the October period) produced by the diffusion operator case DIF2 targeting the DA window from 1 to 11 April (2 to 12 October). The time evolution of each ensemble member for 8-day length could be incorporated for the inflation of the ensemble spread. The ensemble operator C_e was fixed throughout each a4dVar window, but it could represent temporal variability depending on the time of the window, i.e., C_es for the April and October periods are different from each other.

3 Results

3.1 Evaluation of the simulation skills

Reduction ratio of the cost function as compared to that of the first guess generally ranges from 0.6 to 0.7 for each minimization during the target period, and the cost reduction is primarily achieved by a better fit to the SSHA observation. SSI for SSHA increases from 0.777 in the first guess to 0.848–0.882 in the all a4dVar cases (SSHA in Table 3). This demonstrates that there is a room for improvement in SSI by fitting to the SSHA observations at the correct time during the DA window in the forward runs starting from the first guess initial conditions. The first guess produced by ms3dVar includes the satellite altimetry information on maximum 5-day after the time of the initialization depending on the time window for obtaining the assimilative observation data (M17). Fitting to MGDSST data is also improved by the minimization at a lesser extent as shown in SSI of MGDSST in Table 3.

Validation of the products against independent observations also demonstrates skill improvements both for the DA window period (Table 3) and for the succeeding hindcast period (Table 4) as compared to the first guess. For the 10-day DA window period (Table 3), increasing the BEC weight from $c = 0.2$ to $c = 0.5$ in the diffusion operator cases improves SSIs for SSHA, Kuroshio path, and drifter velocities. Dependence of SSI for SLA, IT, and IS on the BEC weight in the diffusion operator cases show no such straightforward increase of the SSIs. Use of the ensemble operator (ENS2) improves SSIs for DFV, IT, and IS as compared to

the diffusion operator case with the same amplitude of the BEC weight (DIF2).

For the succeeding 60-day period, increasing the BEC weight and applying the ensemble operators show complicated responses (Table 4). SSIs for SLA and KPA in the ensemble operator case (ENS2) become worse than those in DIF2, suggesting differences in dynamical responses of the Kuroshio path variations to the modified initial conditions between the diffusion and ensemble operator cases. Dependence on the BEC weight in the diffusion operator indicates saturation of the skill improvements by increasing the weight. Note that SSIs of MGDSST show no sensitivity being at the sufficiently high levels.

According to the skill evaluation described above, we mainly discuss the results of the diffusion operator case DIF3, because the all SSI items outperform those in the first guess (Tables 3 and 4). Figure 2a illustrates that the a4dVar case DIF3 generally improves SSI for SSHA throughout the 70-day period, and shows that the ensemble spread is gradually increasing together with the decline of SSIs. Temporal variations of SSI are different between the Kuroshio Extension, 30º-42ºN and 142º-155ºE (KRE; see Fig. 2 for location), and the Kuroshio, 28º-35ºN and 130º-142ºE (KRS; see Fig. 2 for location), regions. In KRE (Fig. 2b), although the skill improvements are evident at the beginning including the 10-day DA window, the improvements are insignificant in the later period. In KRS (Fig. 2c), the skill improvements persist even in the later period far from the initialization time (Fig. 2c), and the ensemble spread gradually increases after the initialization. Rapid increase of the spread in KRE seems to be related with the rapid decline of SSI (Fig. 2b), suggesting the shorter-time predictability of SSH variations in KRE as compared to those in KRS.

Figure 3 shows temperature increment at 50 m (Fig. 3a, c) and 400 m (Fig. 3b, d) depths at the initialization on 9 April (Fig. 3a, b) and 10 October 2020 (Fig. 3c, d). The changes in temperature are confined in the Subtropical Front, South China Sea, Kuroshio, Kuroshio Extension, and Kuroshio-Oyashio confluence regions characterized by intensive meso-scale eddy activity (Miyazawa et al. 2004). The increments at 50 m depth are more evident than those at 400 m depth in Japan Sea and Kuroshio-Oyashio confluence regions due to the shallower thermocline depth there. The temperature distribution on 10 October is subject to larger corrections (Fig. 3c, d) than that on 9 April (Fig. 3a, b), because the cost function value of the first guess for the October period is about 1.7 times higher than that for the April period. The intensity of the a4dVar increment depends on the data misfit in the first guess. Comparison of temperature distributions at 400 m between the first guess (Fig. 4a, c) and optimized (Fig. 4b, d) initial conditions shows that intensity and locations of Kuroshio path and surrounding
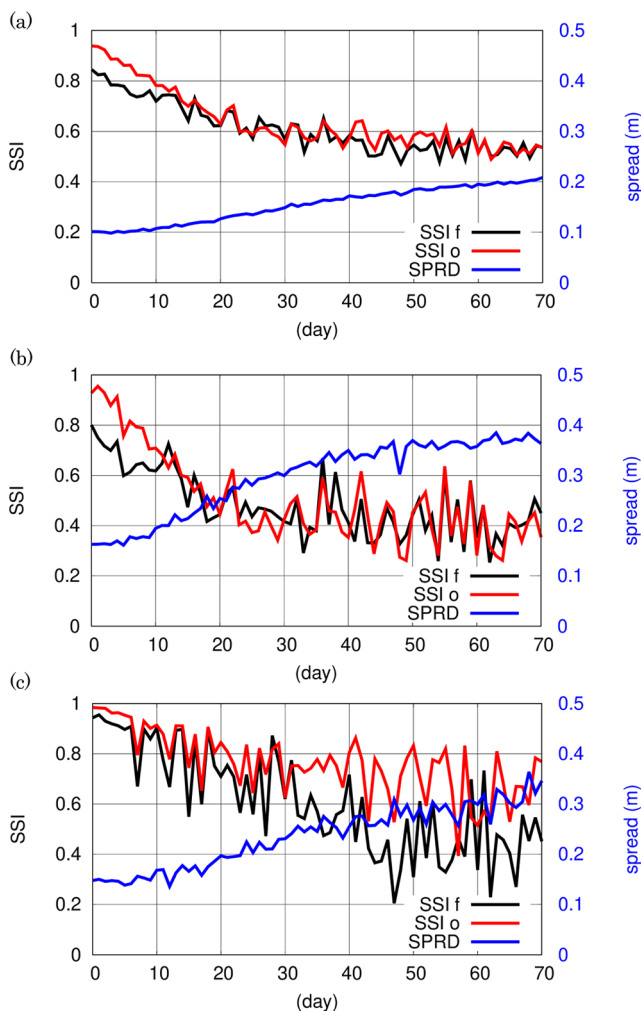
Fig. 2 Composite time sequences of SSI for SSHA averaged over (**a**) the model region, (**b**) Kuroshio Extension region (KRE), 30º-42ºN, 142º-155ºE, and (**c**) Kuroshio region (KRS), 28º-35ºN, 130º-142ºE. Black for the first guess, red for the a4dVar case DIF3. A blue contour denotes an averaged spread of the ensemble simulations

mesoscale eddies are significantly modified by a4dVar. On 9 April, a cyclonic eddy within the core of KLM is slightly weakened and an anticyclonic eddy west of KLM slightly moves westward by a4dVar. On 10 October, a trigger meander around 31°N and 132°E (an offshore anticyclonic eddy around 29°N and 134°E) is weakened (strengthened) and slightly moves eastward (westward).

3.2 Response of the Kuroshio path variations to corrected initial conditions

In April, the hindcast run starting from the first guess shows that KLM disappears after 1 month owing to shedding of a large cyclonic eddy from the tip of KLM (green curves in Fig. 5a, b), but the real KLM persisted throughout this period as indicated by the observed locations (e.g., black curves in

Fig. 5a, b, c). The a4dVar run succeeds in maintaining the KLM shape (red curves in Fig. 5a, b, c) as observed. After 28 May, the large cyclonic eddy detaches off the tip of KLM and again merges with the Kuroshio in the first guess run (not shown).

Positive SSH increments around the Kuroshio path surrounding the KLM core, represented by a local minimum of SSH (see green contours in Fig. 5a), suggest that the intensity of KLM is overestimated by the first guess initial condition. Figure 5a also shows that the a4dVar moved the location of the anticyclonic eddy from 30°N and 134°E northwestward as indicated by positive and negative increments around there.

In October, location of the small meander core changes from 31.5°N and 132.5°E in the first guess (green contours in Fig. 6a) to 32°N and 133.5°E in the a4dVar case (red contours in Fig. 6a), and an offshore anticyclonic eddy core around 29°N and 135°E is displaced northwestward in the a4dVar case compared to the first guess as depicted by positive increments around there. The a4dVar reduces the magnitude of both cold core eddy detached from KLM and the remaining Kuroshio meander as indicated by positive increments in Fig. 6a. The small meander core in the a4dVar run moves to 32°N and 136°E on 12 November, but the small meander in the first guess run keeps its location around 32°N and 133°E (Fig. 6b). On 23 November, the meander slightly moves to 33°N and 134°E in the first guess run but, in contrast to the a4dVar run, does not amplify its magnitude unlike the a4dVar run (Fig. 6c). The small meander again developed into the KLM in January 2021 (not shown). The eastward movement of the small meander related to the coupling behavior of the cyclonic (meander) – anticyclonic (eddy) vortex pairs is also noticed in the KLM formation that occurred in 2004 (Miyazawa et al. 2008).

3.3 Spread-skill variations represented by the a4dVar ensemble

Figures 7a and 8a compare time sequences of SSIs for SSHA south of Japan in April to June (Fig. 7a) and October to December (Fig. 8a). Both cases show that SSIs gradually decline after the initialization and the SSIs of the a4dVar runs outperform those of the first guess runs. After the April period, SSI seems to increase after 28 May 2020, because the large cyclonic eddy once split from the Kuroshio again merges with it in the first guess run, and the resulting Kuroshio path returned back to the KLM as observed. The KLM in the a4dVar run shows similar behavior to the observed Kuroshio path after 28 May (not shown), also leading to the increase of SSI. The amplitude of the ensemble spread from April to June is generally larger than that from October to December. The enhanced amplitude of the spread appears
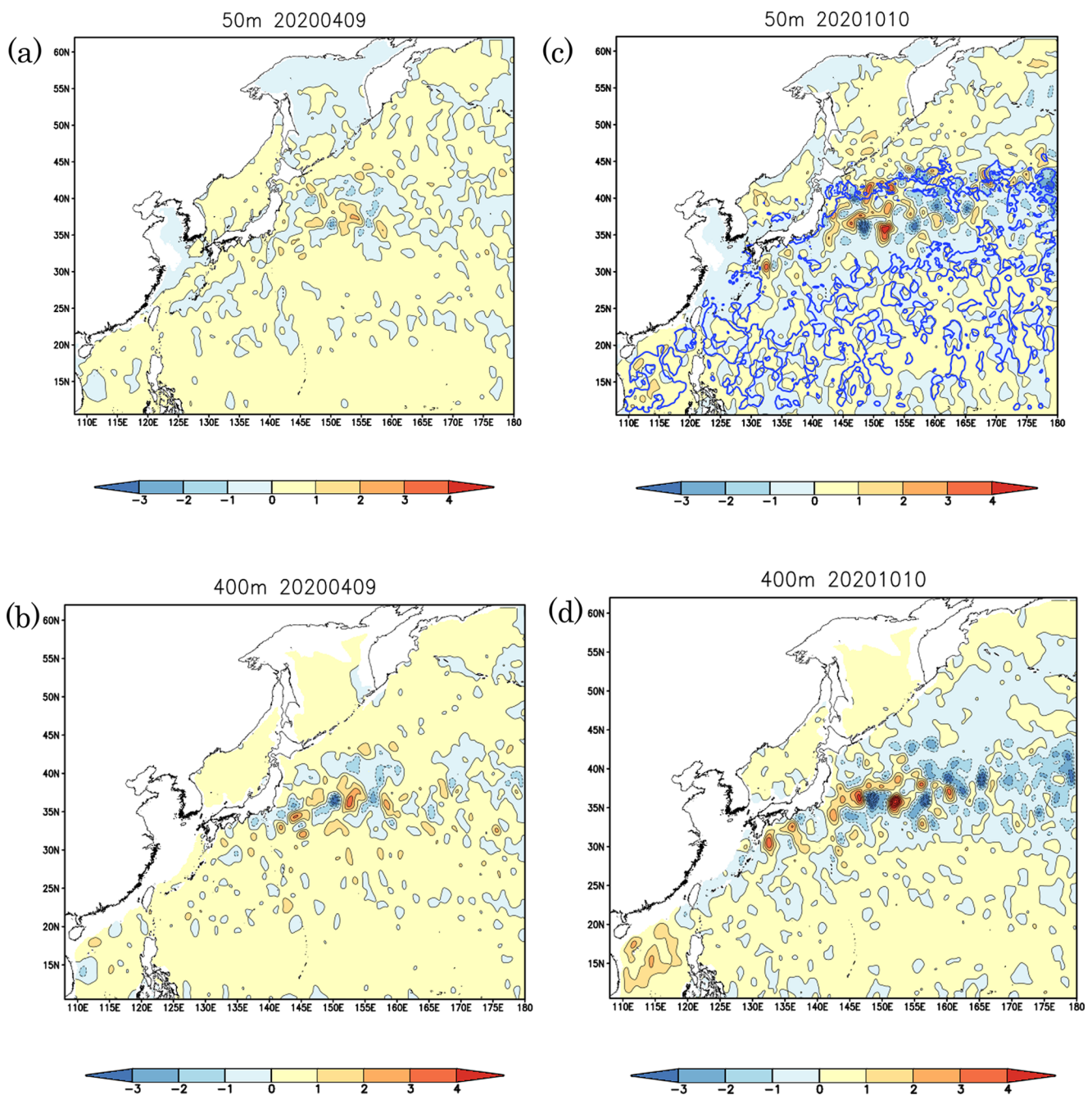
Fig. 3 Changes of the initial condition in temperature (°C) at 50 m (**a**) (**c**) and 400 m (**b**) (**d**) depths in the a4dVar case DIF3. (**a**)(**b**): on 9 April 2020. (**c**)(**d**): on 10 October. The threshold SSH spread contours (M = 1 cm) in (**c**) are shown in blue

around the northern and southern edge of the KLM core (Fig. 7b), suggesting larger variability between the ensemble members related to shedding the cyclonic eddy off KLM. In contrast, the amplitude of the ensemble spread is generally smaller around the Kuroshio south of Japan in November (Fig. 8b) than in May (Fig. 7b). Figure 7 (Fig. 8) shows a combination of lower (higher) skill and larger (smaller) ensemble spread size, inferring possible spread-skill relations represented by the a4dVar ensemble.

The spread-skill correlation is generally significant where temporal variations of spread are considerably large, and spread is basically useful as a predictor of skill when it is extremely large or small as compared to the climatological state of the spread (Whitaker and Loughe 1998). It is thus crucial to know the climatological estimate of the ensemble spread. We need to investigate results of more experiments targeting various events of the Kuroshio path variations for
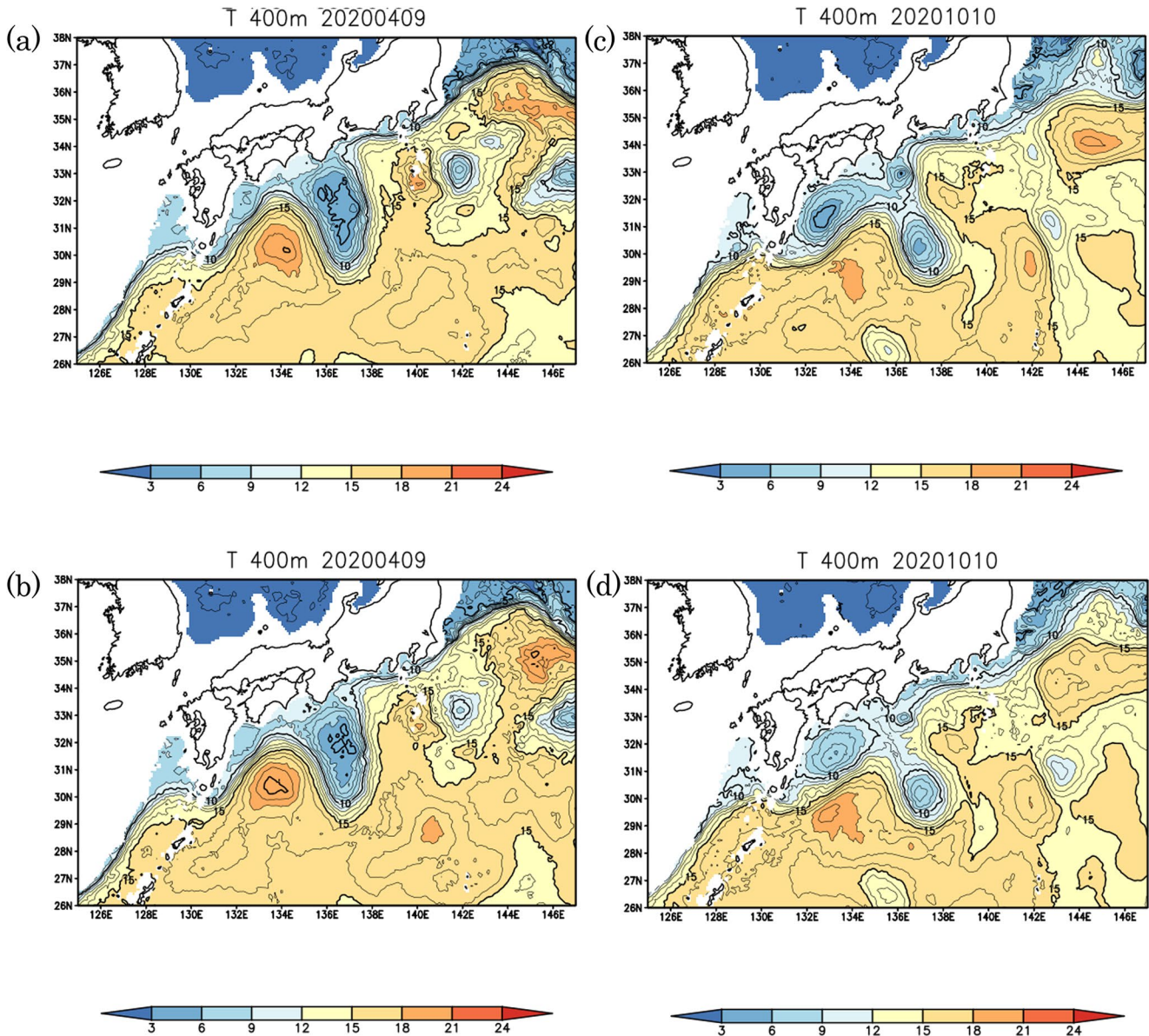
Fig. 4 Snapshots of temperature (°C) at 400 m depth on 9 April 2020. (**a**) The first guess produced by ms3dVar. (**b**) The a4dVar case DIF3. (**c**) As in (**a**) except for 10 October. (**d**) As in (**b**) except for 10 October. Contour interval is 1 degree

detailed identification of the underlying ensemble spread property.

3.4 Effects of the ensemble BECs

Although the average of SSIs in the ensemble BEC case (ENS2) is improved in comparison with the diffusion operator case (DIF2) for the 10-day DA window (Table 3), SSIs of SLA and KPA in ENS2 are considerably low for the 60-day hindcast periods as compared to those in DIF2 (Table 4). Sensitivity of the dynamical responses caused by the Kuroshio path variations triggered by the a4dVar corrections for the two BEC types is shown in Fig. 9 for

the April period. The model run from the first guess initial condition on 9 April (Fig. 9a) generates a westward shift of the Kuroshio path on 25 April (arrow in Fig. 9b). The shift could be caused by a deep anticyclonic circulation around 31.5ºN and 135.5ºE (closed circle in Fig. 9b) as similarly noticed in the enhanced baroclinic instability associated with the KLM formation (Endoh and Hibiya 2001) and it leads to the eddy shedding from KLM in May (green contours in Fig. 5b). The a4dVar cases tend to generally weaken the KLM magnitude by increasing the temperature around KLM (shades in Fig. 9c, e). The Kuroshio path shift and its associated anticyclonic circulation are relatively suppressed as indicated by the decrease of temperature around the
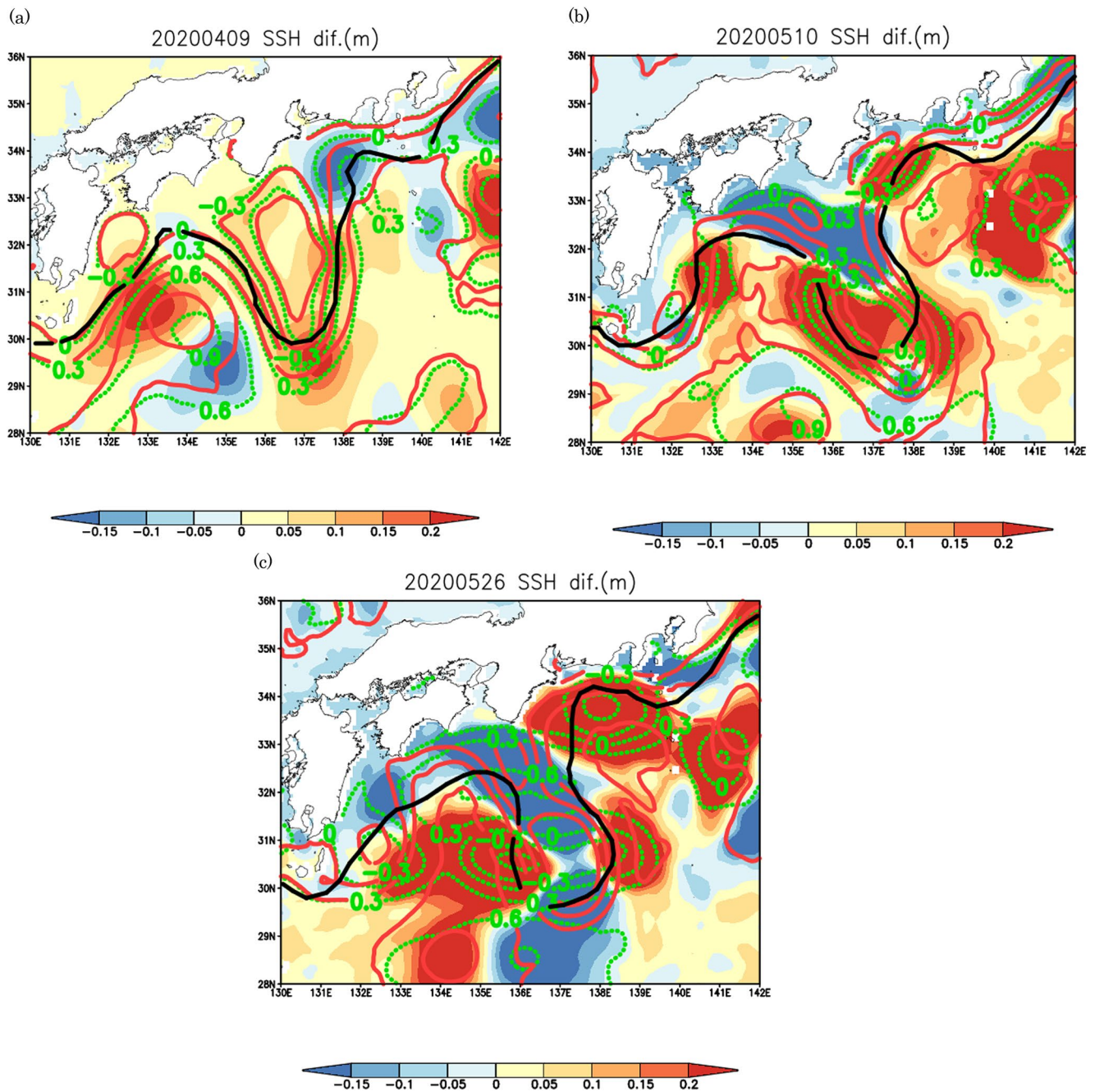
Fig. 5 SSH (m) contours on (**a**) 9 April 2020, (**b**) 10 May 2020, and (**c**) 26 May 2020 with red (green) color of the a4dVar case DIF3 (first guess) initialized on 9 April 2020. Interval is 0.3 m. Shades denote differences in SSH between the a4dVar case DIF3 and first guess. Black contours denote the Kuroshio path locations reported by the Japan Coast Guard

region in the diffusion BEC case (Fig. 9d). But the ensemble BEC case intensifies both shift and anticyclonic circulation (Fig. 9f), and leads to the unrealistic eddy shedding after that (not shown).

To investigate the role of the ensemble BEC in the suggested instability processes, we analyze local energetics using the method applied in Miyazawa et al. (2004). The local energy transfer from the mean kinetic energy to eddy kinetic energy is expressed as follows (Wells et al. 2000),

$$K = - \left[\overline{u'u'} \frac{\partial \overline{u}}{\partial x} + \overline{u'v'} \left(\frac{\partial \overline{u}}{\partial y} + \frac{\partial \overline{v}}{\partial x} \right) + \overline{v'v'} \frac{\partial \overline{v}}{\partial y} \right] \quad (6)$$

where $\overline{u}(\overline{v})$ denotes the eastward (northward) time mean velocity and $u'(v')$ denotes the eastward (northward)
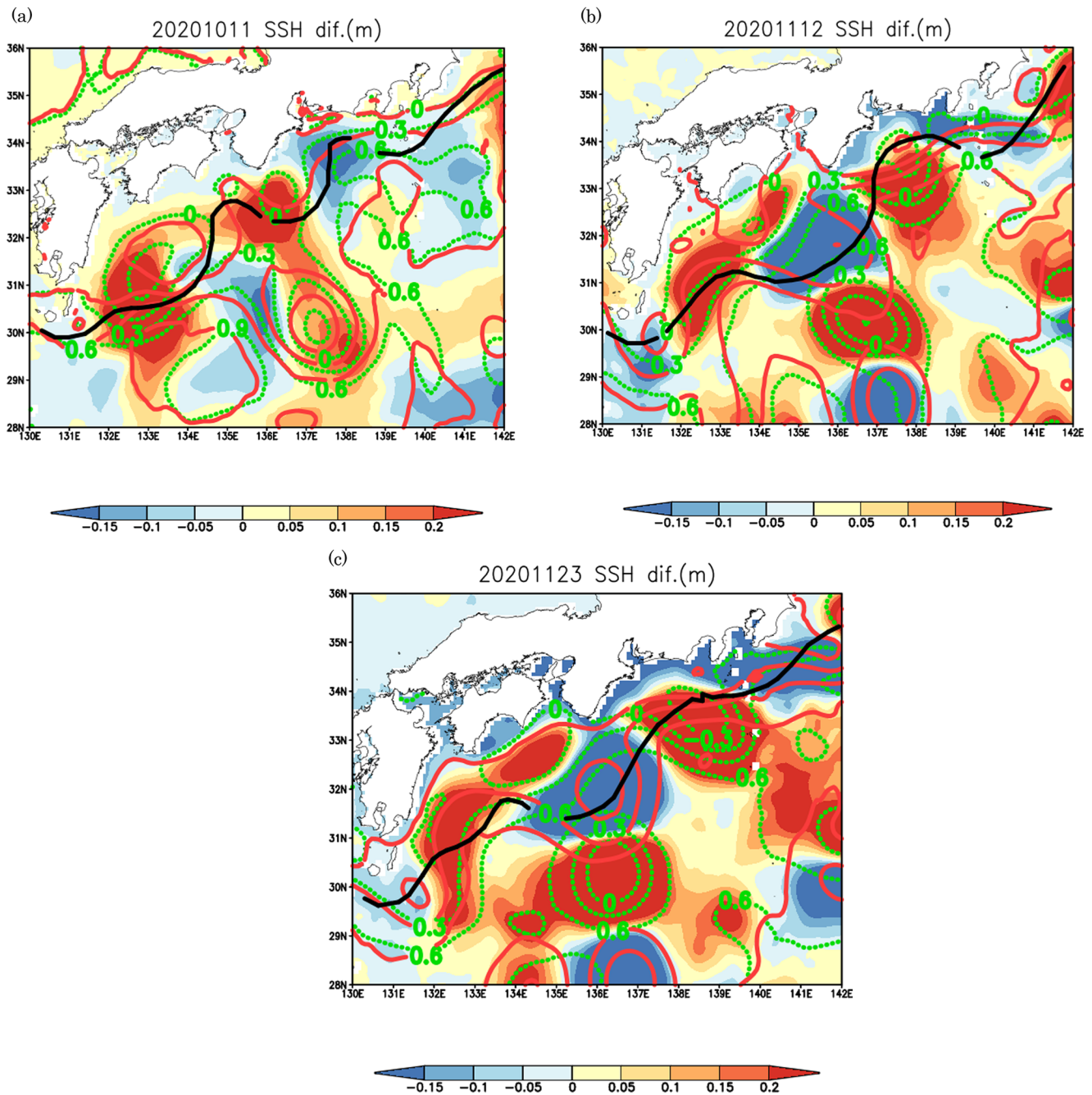
Fig. 6 As in Fig. 5a except for those initialized on (**a**) 10 October 2020. (**b**) 12 November 2020 and (**c**) 23 November 2020

perturbed velocity. The energy transfer from mean potential energy to eddy potential energy is diagnosed by

$$P = -g \left[\frac{\overline{u'\rho'}\frac{\partial\overline{\rho}}{\partial x} + \overline{v'\rho'}\frac{\partial\overline{\rho}}{\partial y}}{\frac{d\rho_b}{dz}} \right] \quad (7)$$

where g is the gravity acceleration, ρ is density, and ρ_b (z) is the background density profile. Figure 10 shows P (left panels) and K (right panels) at 400 m depth for a period

from 21 to 30 April. The first guess case shows a significant positive P patch near the location of the westward shift of the Kuroshio path (Fig. 10a), and it is consistent with the enhanced abyssal currents in the area (Fig. 9b) caused by the baroclinic instability (Endoh and Hibiya 2001). The magnitude of K is relatively small around the KLM core (Fig. 10b). The a4dVar run in the diffusion BEC does not affect the distribution of K (Fig. 10c) and decreases the intensity of the positive values of P around the key region (Fig. 10c). Thereby the eddy shedding does not occur owing

(a)

(a)

(b)

20200526 sprd(m)

(b)

20201119 sprd(m)
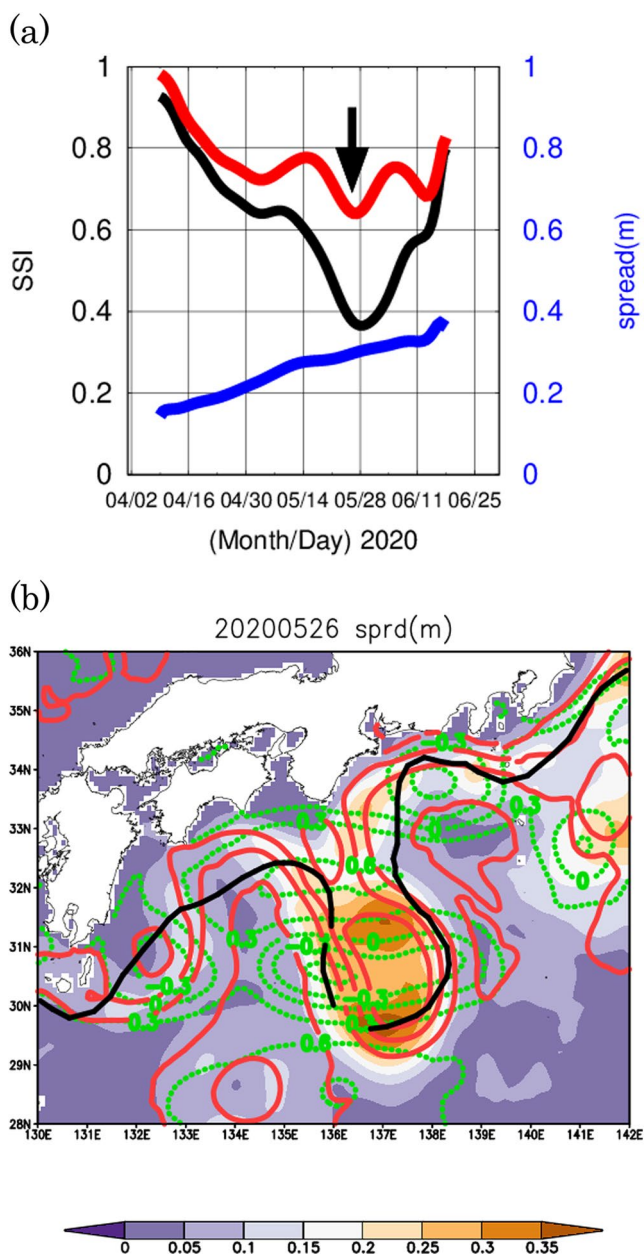
Fig. 7 (**a**) Time sequences of SSI for SSHA (black: the first guess, and red: the a4dVar case DIF3) in the hindcast experiment initialized on 9 April 2020 averaged over the region KRS. A blue curve denotes the ensemble spread. All three curves are smoothed by the Bezier curve fitting. An arrow indicates those on 26 May. (**b**) The SSH ensemble spread (shades) on 26 May of the hindcast experiment. Red (green) contours denote SSH of the a4dVar case DIF3 (first guess). A black curve denotes the Kuroshio path locations reported by the Japan Coast Guard

Fig. 8 (**a**) As in Fig. 7a except for hindcast experiments initialized on 10 October 2020. An arrow indicates 19 November. (**b**) As in Fig. 7b except for a snapshot on 19 November of the hindcast experiments initialized on 10 October

the ensemble BEC case (Fig. 10f). Therefore highly nonlinear eddy shedding processes could be significantly affected by the slight differences in the initial conditions caused by change of the BEC operators.

For the October period, a small meander around 31.5ºN and 132.5ºE shown in the first guess initial condition (Fig. 11a) slightly moves eastward together with amplification of the meander amplitude (Fig. 11b). An excited deep anticyclonic circulation around 31.2ºN and 133.5ºE (closed circle in Fig. 11b) amplifies the unrealistic growth of a trough and ridge (arrow in Fig. 11b) of the small meander through

to the mitigation of the instability processes. The ensemble BEC case shows more reduction of the positive P values around the key region (Fig. 10e) than the diffusion BEC case (Fig. 10c). The horizontal pattern of P in the ensemble BEC case considerably differs from that in the diffusion BEC case, and the intensity of K is generally enhanced in

Fig. 9 Temperature at 400 m depth (contours with an interval of 2 °C) on (**a**, **c**, **e**) 9 April and (**b**, **d**, **f**) 25 April 2020 for (**a**, **b**) the first guess case, (**c**, **d**) the a4dVar case DIF2, and (**e**, **f**) the a4dVar case ENS2. An arrow in (**b**) indicates the westward shift of the Kuroshio path, and a solid circle indicates the center of the excited deep anticyclonic circulation. Shades in (c-f) denote temperature differences in comparison to the first guess. A square in (**f**) denotes an area (30.5 °-32.5 °N, 134 0.5°-137 0.5°E) showing an area of the excited deep anticyclonic circulation. Vectors in (**b**, **d**, **f**) denote ocean currents at 3000 m depth on 25 Apr with velocity magnitude greater than 0.15 ms^{-1}
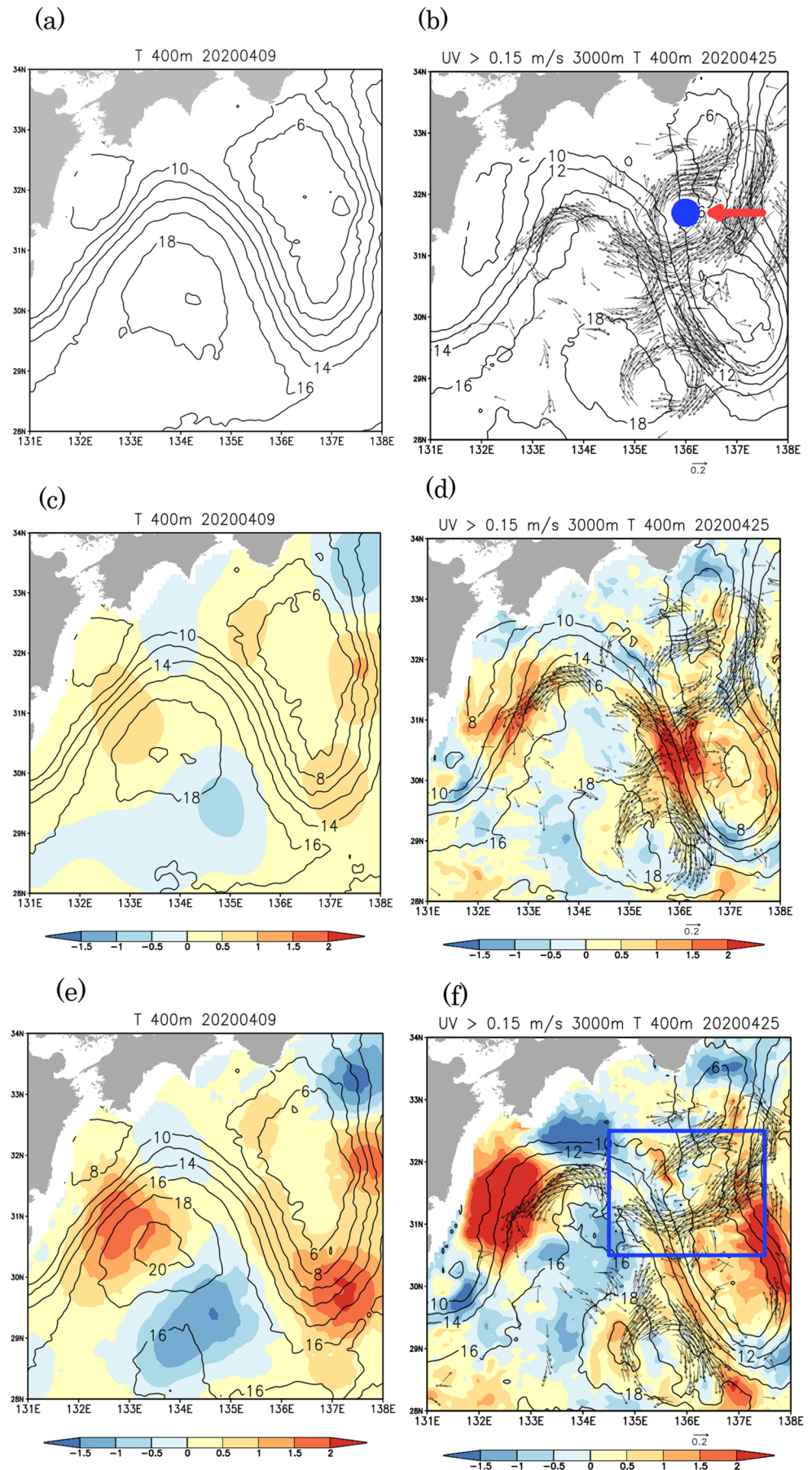
Fig. 10 The baroclinic energy transfer term P (Eq. 7) (**a**, **c**, **d**) and barotropic energy transfer term K (Eq. 6) (**b**, **d**, **f**) at 400 m depth for a period from 21 to 30 April 2020 denoted by shades in 10^{-6} m^2 s^{-3}. (**a**) (**b**): the first guess case. (**c**) (**d**): the a4dVar case DIF2. (**e**) (**f**): the a4dVar case ENS2. Contours denote temperature at 400 m depth with an interval of 1 °C. Arrows in (**a**) (**b**) denote the westward shift of the Kuroshio path
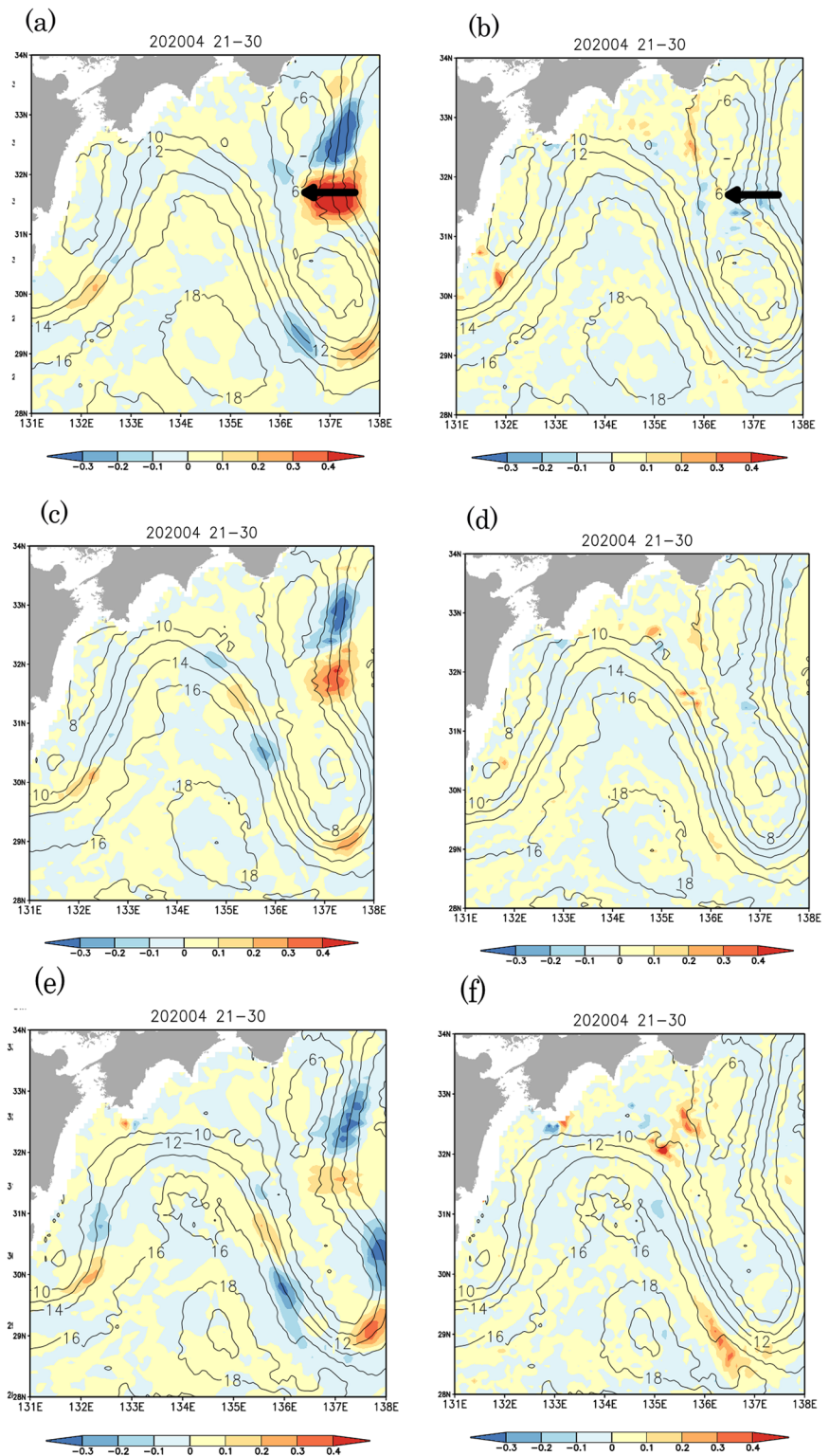
baroclinic instability (Endoh and Hibiya 2001). The small meander in the first guess run eventually fades away without moving northeastward as indicated by the green contours in Fig. 6b, c, though the a4dVar run represents northeastward movement of the meander (red contours) as observed (black contours). The a4dVar corrections weaken the amplitude of the small meander by increasing temperature mainly around the upstream side (shades in Fig. 11c, e). They facilitate the northeastward movement of the meander (Fig. 11d, f), and decrease the intensity of the deep anticyclonic circulation.

Fig. 11 As in Fig. 9 except for 10 October 2020 (**a**, **c**, **e**) and for 25 October (**b**, **d**, **f**). An arrow in (**b**) denotes a ridge side of the amplified meander, and a solid circle indicates the center of the deep anticyclonic circulation. A square in (**f**) indicates an area of rise in temperature associated with the northeastward moving the small meander, 31 °-32 °N and 134 °-135 °E
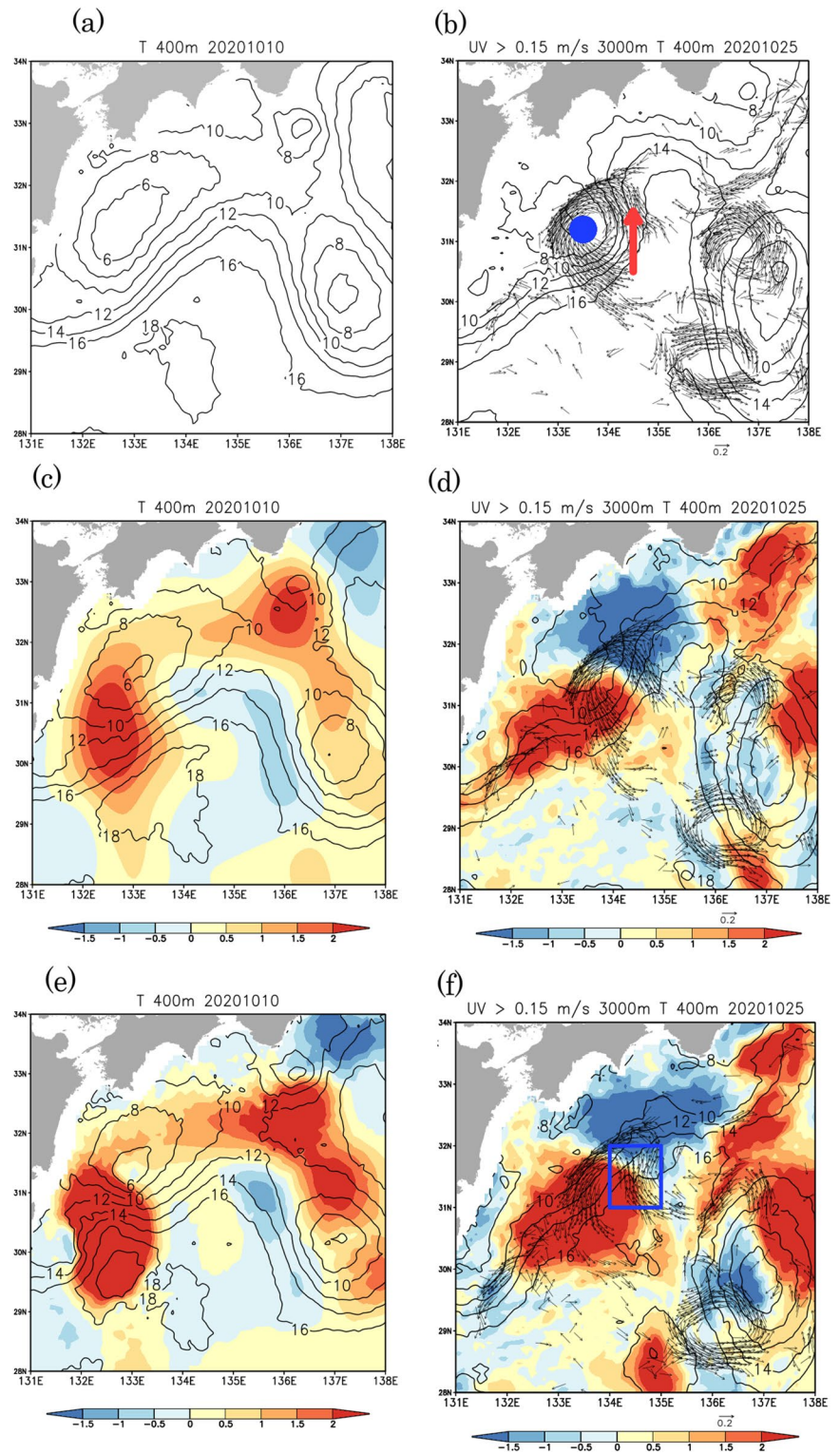
Applying the ensemble BEC seems to emphasize this tendency (Fig. 11f). The small meander moves northeastward faster than the observed one (not shown) in the ensemble BEC case.

The instability analysis during the October period shows that the diffusion BEC case decreases the intensity of both P and K (Fig. 12c, d) compared to those in the first guess (Fig. 12a, b). The changes in the initial condition due to the switch to the ensemble BEC operator facilitate the

Fig. 12 As in Fig. 10 except for a period from 21 to 30 October 2020. Arrows in (**a**) (**b**) denote a ridge side of the amplified meander
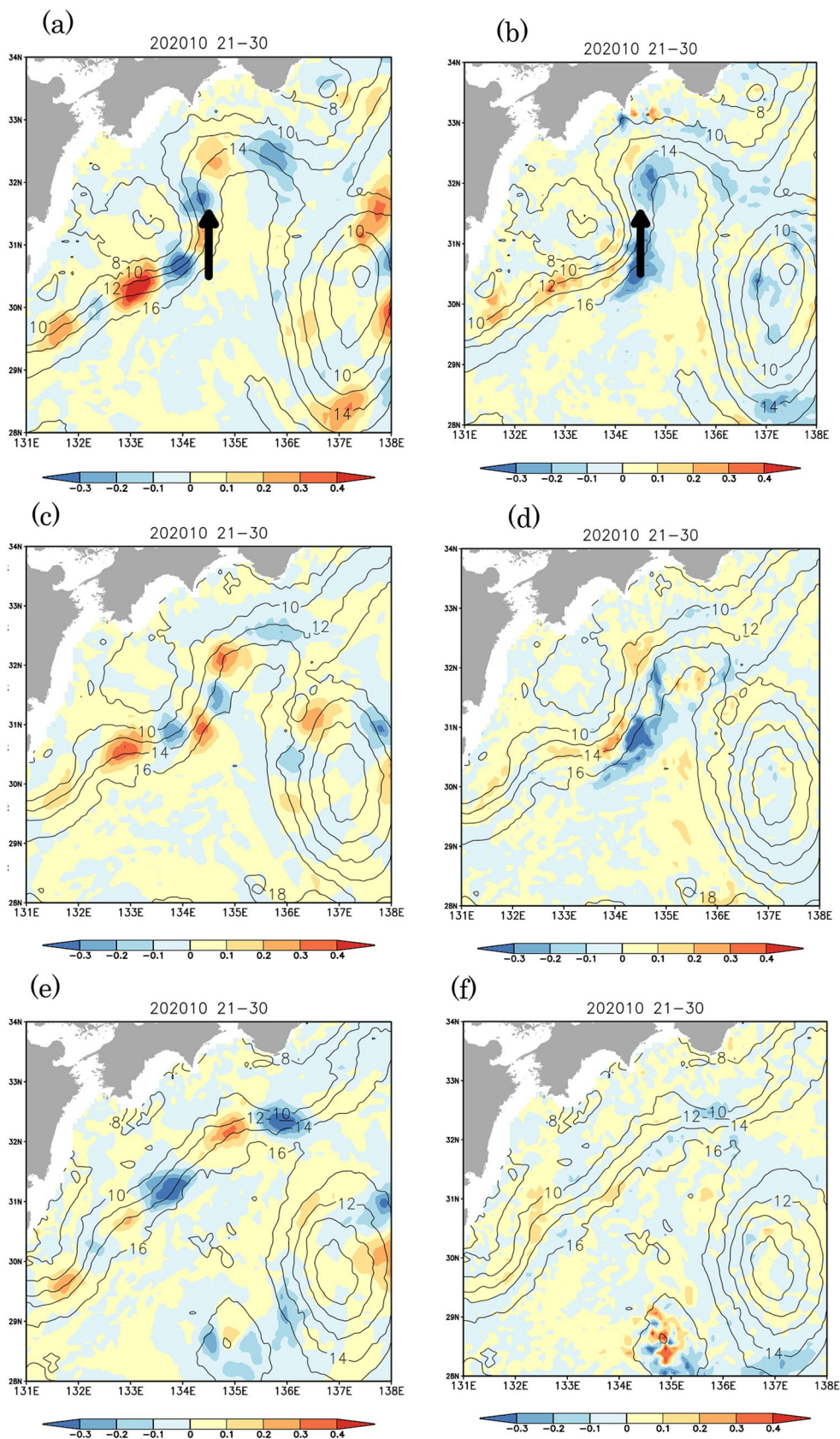
downstream movement of the small meander and suppress the instability processes associated with the evolution of the small meander (Fig. 12e, f).

The initial conditions in the ensemble BEC case tend to have locally exaggerated increments (Figs. 9e and 11e) compared to those in the diffusion BEC case (Figs. 9c and 11c). This leads to unrealistic dynamical responses in the succeeding simulations, as shown in Figs. 9f and 11f, resulting in a decline of the SSIs related to the Kuroshio path variation south of Japan, as presented in Table 4.

To detect possible origins of the incorrect dynamical responses of the Kuroshio path variations, we evaluate sensitivity to the initial conditions represented by the ensemble BEC case. Here we apply the ensemble sensitivity analysis based on regression of the ensemble perturbed around the targeted events (Enomoto et al. 2015; Aoki et al. 2020). The ensemble regression (ER) of ensemble anomaly vectors $\mathbf{X}(t)$ at a time t to an ensemble target quantity vector $\mathbf{Y}(t0)$ at a targeted time $t0$ ($t0 > t$) is represented as,

$$\mathbf{ER}(t) = \mathbf{X}(t)\left(\mathbf{X}(t)^t\mathbf{X}(t)\right)^{-1}\mathbf{Y}(t0) \qquad (8)$$

For the April period, we regress the intensity of the deep anticyclonic circulation excited in the ensemble BEC case (Fig. 9f) on the increments in the temperature initial condition (Fig. 9e). $\mathbf{Y}(t0)$ is defined as m_s-dimensional vector containing the numbers of grids with velocity magnitude at 3000 m depth exceeds 0.3 m/s within a square region of 30.5º-32.5ºN and 134.5º-137.5ºE (see square in Fig. 9f) on $t0 =$ April 25th. $\mathbf{X}(t)$ are the ensemble anomaly vectors of temperature at 400 m depth on time t for a period from 9 to 25 April. A statistically significant region appearing on the closest day to the initialization day (9 April) is detected on 11 April as denoted by an arrow in Fig. 13a. The signal corresponds to the positive increment around the tip of KLM (Fig. 9e on 9 April). The signal moves northward (Fig. 13b) along the Kuroshio path slightly shifting westward (Fig. 13c), and arrives at the targeted region (Fig. 13d) where the deep anticyclonic circulation is strengthened (see square in Fig. 9f). The signals detected on 20 (Fig. 13c) and on 25 (Fig. 13d) April seems to be consistent with the positive values of P and K around the signal area for the period from 21 to 30 April.

Figure 14 shows the ER signals for the October period. $\mathbf{Y}(t0)$ contains the numbers of grid points with temperature at 400 m exceeding 15ºC within a square region of 31º-32ºN and 134º-135ºE (see square in Fig. 11f) on 25 October, while $\mathbf{X}(t)$ are the ensemble anomaly vectors of temperature at 400 m for a period from 10 to 25 October. Statistically significant regions are detected on 11 October (arrow in Fig. 14a) 1-day after the initialization day (10 October). It is related to the enhanced temperature gradient along the

front of the Kuroshio path (Fig. 14a). The sensitive region moves northeastward that is accompanied by the moving small meander (Fig. 14b, c, d).

4 Discussion

The a4dVar operation corrects overestimation of the KLM amplitude and prevents the unrealistic eddy shedding from KLM during the 60-day hindcast for the April period. The wavelength λ of KLM is generally governed by the inflow U_0 as $\lambda = (U_0/\beta)^{1/2}$ where β is the meridional differential of the Coriolis coefficient (White and McCreary 1976). If λ is larger than that expected from the inflow U_0, KLM would be unstable. Any disturbance could lead to eddy shedding from KLM by amplifying it. The a4dVar dynamically corrects the amplitude/wavelength of KLM to balance it with the underlying Kuroshio flow. It mainly changes the baroclinic conditions through the geostrophic balance operator $\mathbf{L}$ in BEC (Eq. 2) and hardly affects the barotropic transport conditions. Note that locally much enhanced increment could induce the disturbance causing the eddy shedding as demonstrated by the ensemble BEC case (Fig. 9f). The ensemble regression analysis clearly detects the location of the locally enhanced increment created by the ensemble BEC (Fig. 13a).

For the October period, the a4dVar weakens the amplitude/wavelength (λ) of the small meander and further intensifies the horizontal gradient of the Kuroshio path along the meander. The first guess represents a relatively balanced condition of λ and U_0 close to $\lambda = (U_0/\beta)^{1/2}$, and results in near-stagnation of the meander (Fig. 11b). The a4dVar corrects both λ and U_0, resulting in a more realistic motion speed of the meander as observed (Fig. 6). Again, during this period, the locally enhanced correction in the ensemble BEC case results in the faster motion of the meander (Fig. 11f) than that expected from the observations. The localized gradient generated by the ensemble BEC along the southern boundary of the small meander (Fig. 11e) is identified by the ensemble regression analysis as indicated by the statistically significant area (arrow in Fig. 14a).

The modification of the prescribed BEC represented by the diffusion operator utilizing the ensemble information improves the SSIs for temperature and salinity distributions (Tables 3 and 4). The horizontally fine structures of temperature and salinity that can be represented by the ensemble BEC (Miyazawa et al. 2012, 2013) improve SSIs to fit the temperature and salinity data. The SSIs for sea levels and Kuroshio path variations deteriorate, because the resulting locally enhanced and/or too steep horizontal gradient in the initial conditions distort the underlying dynamics of ocean current variations. However, the Kuroshio path variation,
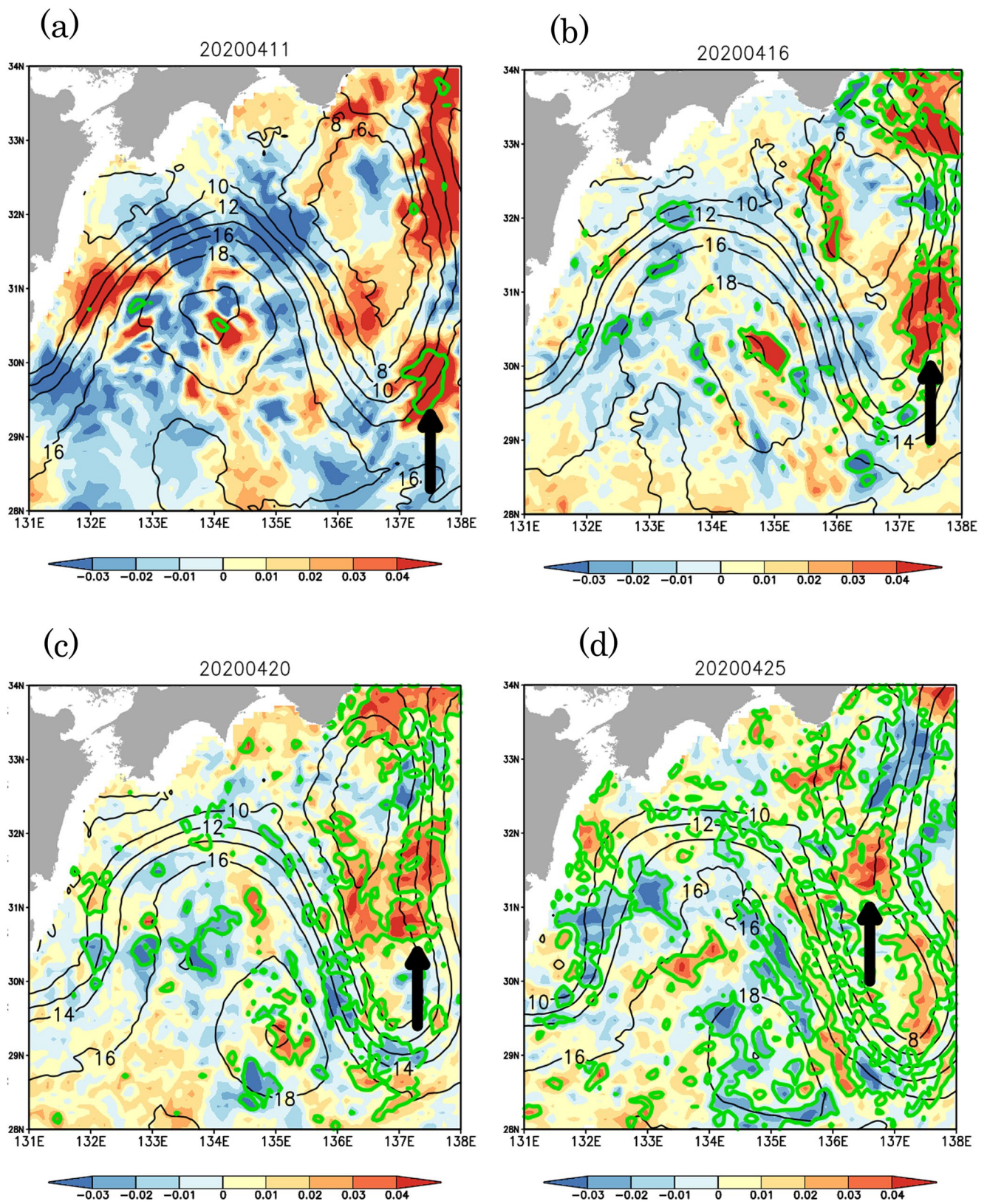
Fig. 13 The ensemble regression (shade) of temperature at 400 m on (**a**) 11 April 2020, (**b**) 16 April 2020 and (**c**) 25 April 2020 to the excited anticyclonic circulation on 25 April in the region of 30.5 °-32.5 °N and 134 0.5°-137 0.5°E (see square in Fig. 9f) in the hindcast experiment that initialized on 9 April of the a4dVar case ENS2.

The ensemble mean temperature at 400 m depth is denoted by black contours with an interval of 2 °C. Green contours show statistically significant areas with 95% confidence intervals (e.g., Sect. 6.2.5. in Wilks 2005). An arrow denotes a sensitive region to the excited deep anticyclonic circulation on 25 April
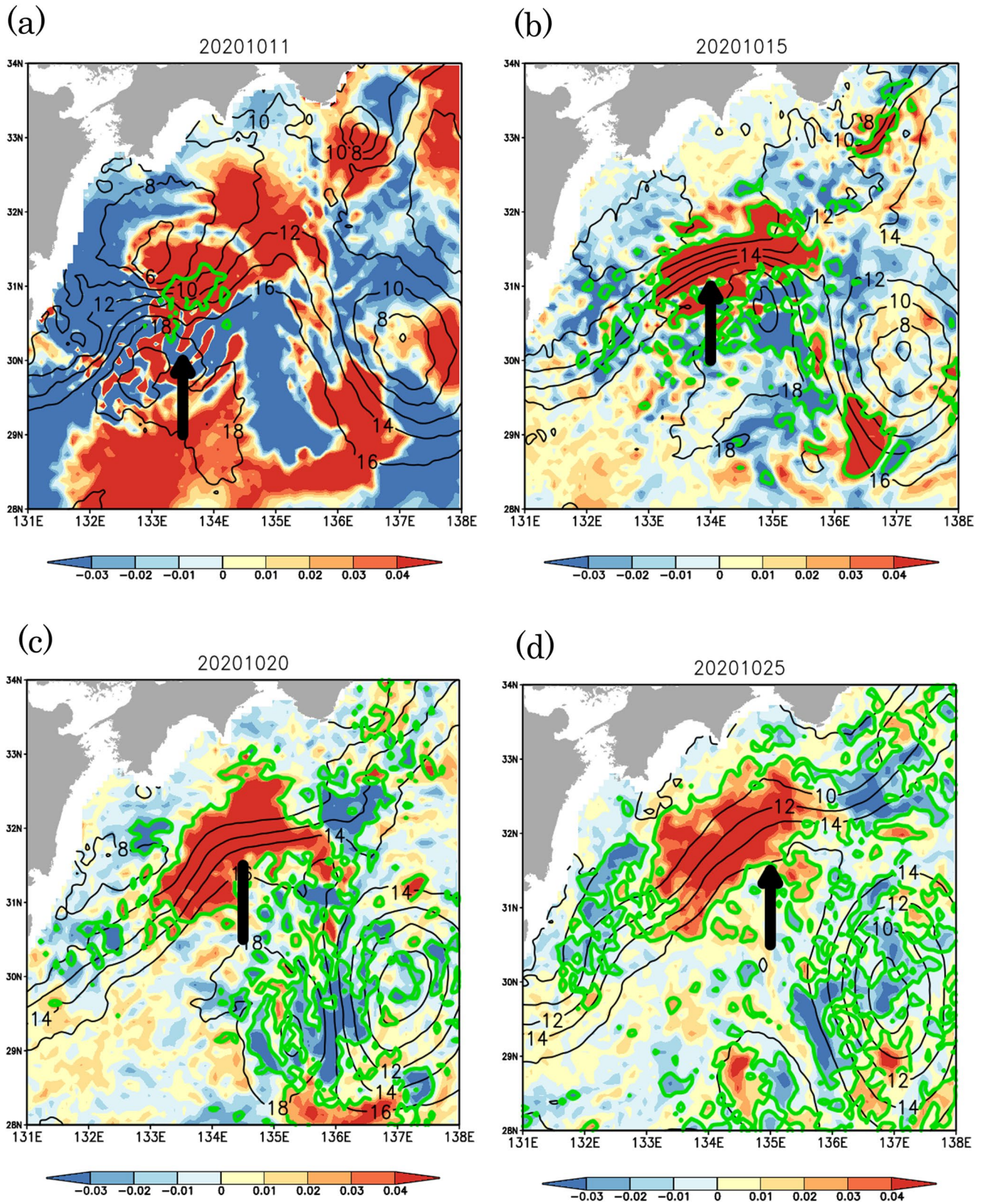
Fig. 14 The ensemble regression (shade) of temperature at 400 m on (**a**) 11 October 2020, (**b**) 15 October 2020, (**c**) 20 October 2020, and (**d**) 25 October 2020 to temperature at 400 m exceeding 15ºC on 25 October in the region of 31°-32°N and 134°-135°E (see square in Fig. 9f) in the hindcast experiment that initialized on 10 October of the a4dVar case ENS2. The ensemble mean temperature at 400 m depth is denoted by black contours with an interval of 2 °C. Green contours show statistically significant areas with 95% confidence intervals. Arrows denote sensitive regions to rise in temperature associated with the northeastward moving of the small meander on 25 October 2020

including the eddy-current interactions, is governed by the highly nonlinear dynamics. Slight changes in the initial conditions lead to significant variability through instability processes as demonstrated in the April case (Fig. 10). Eddy-current interactions are strongly influenced by sub-grid parameterization schemes, including horizontal/vertical viscosity/diffusivity operators as demonstrated by Oey (1996) in the case of Loop Current eddy shedding in the Gulf of Mexico. In the future, it will be necessary to investigate the sensitivity of the forecast skill to parameterization of the BEC operators in various sub-grid parameterization settings.

Unlike other ensemble-based methods (e.g., Liu et al. 2008), a4dVar does not require the model ensemble specification for estimating BEC, and the inclusion of the ensemble BEC in the present study does not yield a significant improvement of the skill. However, representation of flow-dependent error covariance based on the ensemble could be effective for assimilating new wide-swath altimetry data (Rodriguez et al. 2017) in the future applications. More detailed studies about the design of the ensemble BEC with possible larger sizes of ensemble based on the detailed analysis of more other Kuroshio path variation events are required for further utilizing the ensemble BEC. Also, other directions of utilizing ensemble information including the spread-skill correlations and ensemble sensitivity, both which are preliminary applied in the present study, will be further investigated in the future studies.

5 Summary

We have introduced correction of the initial conditions in an operational Northwest Pacific Ocean state forecast system by applying a previously developed adjoint-free 4dVar scheme (M20). The correction is applied to the first guess initial conditions produced by the ms3dVar scheme (M17), resulting in a significantly better fit of the model trajectory to the time-dependent altimetry observations during the 10-day DA window. Major changes in the subsurface oceanic fields occur around the depth of the main thermocline (400 m) in the South China Sea, Kuroshio, Kuroshio Extension, and Kuroshio-Oyashio confluence regions, where significant meso-scale eddy activity is well observed by the satellite altimetry.

System validation against independent data confirms that the a4dVar correction significantly (~40%) improves SSIs of the sea level, the Kuroshio path south of Japan, drifter velocities, and in-situ temperature and salinity distributions not only during the 10-day DA window but also during the succeeding 60-day hindcast periods. The correction by a4dVar redistributes the magnitudes and locations of the

meanders resulting in more accurate representation of the relevant phenomena including eddy detachment from the tip of KLM and eastward movement of the Kuroshio small meander which triggered the KLM regeneration during the analyzed period. The dynamical balance between the meander amplitude/wavelength and flow advection corrected by a4dvar affects the dynamical response of the Kuroshio path variations.

The actual elapsed time for 10 iterations of 10-day DA window with 22 ensemble members using both ensemble and diffusion BEC operators was around 4–5 h using 1402 vector cores of the 4th generation Earth Simulator based on NEC SX-Aurora TSUBASA at Japan Agency for Marine-Earth Science and Technology (JAMSTEC). We are currently preparing near real-time operation of the developed ensemble forecast system of the Northwest Pacific. In the near future, an updated forecast information including the ensemble of oceanic states will be available on our website: https://www.jamstec.go.jp/jcope/.

Declarations

References

Anderson JL, Anderson SL (1999) A Monte Carlo implementation of the nonlinear filtering problem to produce ensemble assimilations and forecasts. Mon Wea Rev 127:2741–2758

Aoki K, Miyazawa Y, Hihara T, Miyama T (2020) An objective method for probabilistic forecasting of multimodal Kuroshio states using ensemble simulation and machine learning. J Phys Oceanogr 50:3189–3204

Bell MJ, Lefebvre M, le Traon P-Y, Smith N, Wilmer-Becker K (2009) GODAE: The Global Ocean Data Assimilation Experiment. Oceanography 22:14–21

Conkright ME, Locarnini RA, Garcia HE, O'Brien TD, Boyer TB, Stephens C, Antonov JI (2002) World Ocean Atlas 2001: objective analyses, Data statistics, and figures, CD-ROM documentation. National Oceanographic Data Center, Silver Spring, MD, p 17

Endoh T, Hibiya T (2001) Numerical simulation of the transient response of the Kuroshio leading to the large meander formation south of Japan. J Geophys Res Oceans 106:26833–26850

Enomoto T, Yamane S, Ohfuchi W (2015) Simple sensitivity analysis using ensemble forecasts. J Met Soc Jpn 93:199–213

Ezer T, Mellor GL (1994) Continuous assimilation of Geosat altimeter data into a primitive equation Gulf Stream model. J Phys Oceanogr 24:832–847

Fujii Y, Kamachi M, Hirose N, Mochizuki T, Setou T, Miyama T, Hirose N, Osafune S, Han S, Igarashi H, Miyazawa Y, Toyoda T, Hoshiba Y, Masuda S, Ishikawa Y, Usui N, Kuroda H, Takayama K (2017) Japanese studies of ocean data assimilation: milestones over the past 20 years and future perspectives. Oceanogr Japan 26:15–43 (in Japanese with English abstract and figure captions)

Furuichi N, Hibiya T, Niwa Y (2012) Assessment of turbulence closure models for resonant inertial response in the oceanic mixed layer using a large eddy simulation model. J Oceanogr 68:285–294

Gaspari G, Cohn SE (1999) Construction of correlation functions in two and three dimensions. Q J Royal Met Soc 554:723–757

Hamill TM, Snyder C (2000) A hybrid ensemble Kalman filter – 3D variational analysis scheme. Mon Weather Rev 128:2905–2919

Hanawa K, Mitsudera H (1985) About the daily averaging method of oceanic data (in Japanese). Bull Coastal Oceanogr 23:79–87

Hirose N, Fukumori I, Kim C-H, Yoon J-H (2005) Numerical simulation and satellite altimeter data assimilation of the Japan Sea circulation. Deep Sea Res II 52:1443–1463

Kawabe M (1989) Sea level changes south of Japan associated with the non-large-meander path of the Kuroshio. J Oceanogr Soc Jpn 45:181–189

Kurihara Y, Sakurai T, Kuragano T (2006) Global daily sea surface temperature analysis using data from satellite microwave radiometer, satellite infrared radiometer and in-situ observations. Weather Service Bullet 73(Special issue):s1–s18 (in Japanese)

Li Y, Gao Z, Lenschow DH, Chen F (2010) An improved approach for parameterizing surface layer turbulent transfer coefficients in numerical models. Bound Layer Meteorol 137:153–165

Liu C, Xiao Q, Wang B (2008) An ensemble-based four-dimensional variational data assimilation scheme. Part I: technical formulation and preliminary test. Mon Weather Rev 136:3363–3373

Lumpkin R, Centurioni L (2019) Global Drifter Program quality-controlled 6-hour interpolated data from ocean surface drifting buoys. https://doi.org/10.25921/7ntx-z961. NOAA National Centers for Environmental Information. Dataset

Mellor GL, Hakkinen S, Ezer T, Patchen R (2002) A generalization of a sigma coordinate ocean model and an inter comparison of model vertical grids. In: Pinardi N, Woods JD (eds) Ocean forecasting: conceptual basis and applications. Springer, New York, pp 55–72

Miyazawa Y, Guo X, Yamagata T (2004) Roles of meso-scale eddies in the Kuroshio paths. J Phys Oceanogr 34:2203–2222

Miyazawa Y, Yamane S, Guo X, Yamagata T (2005) Ensemble forecast of the Kuroshio meandering. J Geophys Res 110:C10026

Miyazawa Y, Kagimoto T, Guo X, Sakuma H (2008) The Kuroshio large meander formation in 2004 analyzed by an eddy-resolving ocean forecast system. J Geophys Res 113:C10015

Miyazawa Y, Zhang RC, Guo X, Tamura H, Ambe D, Lee JS, Okuno A, Yoshinari H, Setou T, Komatsu K (2009) Water mass variability in the Western North Pacific detected in a 15-year eddy resolving ocean reanalysis. J Oceanogr 65:737–756

Miyazawa Y, Miyama T, Varlamov SM, Guo X, Waseda T (2012) Open and coastal seas interactions south of Japan represented by an ensemble Kalman Filter. Ocean Dyn 62:645–659

Miyazawa Y, Murakami H, Miyama T, Varlamov SM, Guo X, Waseda T, Sil S (2013) Data assimilation of the high-resolution sea surface temperature obtained from the Aqua-Terra satellites (MODIS-SST) using an ensemble Kalman filter. Remote Sens 5:3123–3139

Miyazawa Y, Varlamov SM, Miyama T, Guo X, Hihara T, Kiyomatsu K, Kachi M, Kurihara Y, Murakami H (2017) Assimilation of high-resolution sea surface temperature data into an operational nowcast/forecast system around Japan using a multi-scale three-dimensional variational scheme. Ocean Dyn 67:713–728

Miyazawa Y, Kuwano-Yoshida A, Doi T, Nishikawa H, Narazaki T, Fukuoka T, Sato K (2019) Temperature profiling measurements by sea turtles improve ocean state estimation in the Kuroshio-Oyashio confluence region. Ocean Dyn 69:267–282

Miyazawa Y, Yaremchuk M, Varlamov SM, Miyama T, Aoki K (2020) Applying the adjoint-free 4dVar assimilation to modeling the Kuroshio south of Japan. Ocean Dyn 70:1129–1149

Miyazawa Y, Varlamov SM, Miyama T, Kurihara Y, Murakami H, Kachi M (2021) A nowcast/forecast system for Japan's coast using daily assimilation of remote sensing and in situ data. Remote Sens 13:2431

Nakanishi M, Niino H (2009) Development of an improved turbulence closure model for the atmospheric boundary layer. J Metorol Soc Jpn 87:895–912

Oey LY (1996) Simulation of mesoscale variability in the Gulf of Mexico: sensitivity studies, comparison with observations, and trapped wave propagation. 26:145–175

Ohishi S, Miyoshi T, Kachi M (2023) LORA: a local ensemble transform Kalman filter-based ocean research analysis. Ocean Dyn 73:117–143

Pasmans I, Kurapov AL, Barth JA, Kosro PM, Shearman K (2020) Ensemble 4DVAR (En4DVar) data assimilation in a coastal ocean circulation model. Part II: Implementation offshore Oregon–Washington, USA. Ocean Modelling 154: 101681

Paulson CA, Simpson JJ (1977) Irradiance measurements in the upper ocean. J Phys Oceanogr 7:952–956

Rodriguez E, Fernadez DE, Peral E, Chen CW, Bleser J-W, Williams B (2017) WIde-Swath Altimetry A Review. In: Satellite altimetry over oceans and land surfaces. Stammer D, Cazenave A (Eds) CRC press 71–112

Saha S, Moorthi S, Wu X, Wang J, Nadiga S, Tripp P, Behringer D, Hou Y-T, Chuang H-y, Iredell M, Ek M, Meng J, Yang R, Mendez MP, Dool Hvd, Zhang Q, Wang W, Chen M, Becker E (2014) The NCEP climate forecast system version 2. J Clim 27:2185–2208

Sato Y, Horiuchi K (2022) Energy-saving voyage by utilizing the ocean current. IoS-OP Taiwan Seminar – Archives On-demand No. 19 https://www.shipdatacenter.com/en/ios-op_seminar_twod_202208 (accessed on 12 August 2022)

Usui N, Fujii Y, Sakamoto K, Kamachi M (2015) Development of a four-dimensional variational assimilation system for coastal data assimilation around Japan. Mon Wea Rev 143:3874–3892

Varlamov SM, Miyazawa Y (2021) High-performance computing of ocean models for Japan Coastal Ocean Predictability Experiment: a parallelized sigma-coordinate ocean circulation model JCOPE-T. Annu Rep Earth Simulator April 2020-Feb 2021 1–3

Wells NC, Ivchenko VO, Best SE (2000) Instabilities in the Agulhas Retroflection current system: a comparative model study. J Geophys Res 105:3233–3241

Whitaker JS, Hamill TM (2012) Evaluating methods to account for system errors in ensemble data assimilation. Mon Wea Rev 140:3078–3089

Whitaker JS, Loughe AF (1998) The relationship between ensemble spread and ensemble mean skill. Mon Wea Rev 126:3292–3302

White WB, McCreary JP (1976) On the formation of the Kuroshio meander and its relationship to the large-scale ocean circulation. Deep Sea Res Oceanogr Abstracts 23:33–47

Wilks DS (2005) Statistical methods in the Atmospheric sciences. Elsevier Academic, p 648

Willmott CJ (1981) On the validation of models. Phys Geogr 2:184–194

Yaremchuk M, Martin P, Koch A, Beattie C (2016) Comparison of the adjoint and adjoint-free 4dVar assimilation of the hydrographic and velocity observations in the Adriatic Sea. Ocean Model 97:129–140

Yaremchuk M, Martin P, Beattie C (2017) A hybrid approach to generating search subspaces in dynamically constrained 4-dimensional data assimilation. Ocean Model 117:41–51